POLITECNICO DI TORINO
Repository ISTITUZIONALE

Strength and Ductility of Hybrid Steel and FRP Reinforced Concrete Sections Subjected to Combined Axial and Bending Regime

Original
Strength and Ductility of Hybrid Steel and FRP Reinforced Concrete Sections Subjected to Combined Axial and Bending Regime / Mairone, M., Maragno, G., Masera, D., Corrado, M.. - In: INFRASTRUCTURES. - ISSN 2412-3811. - 11:5(2026), pp. 1-37. [10.3390/infrastructures11050170]

Availability:
This version is available at: 11583/3011317 since: 2026-05-23T20:35:15Z

Publisher:
MDPI

Published
DOI:10.3390/infrastructures11050170

Terms of use:

This article is made available under terms and conditions as specified in the corresponding bibliographic description in the repository

Publisher copyright

(Article begins on next page)

01 November 2026

infrastructures

MDPI

Article

Strength and Ductility of Hybrid Steel and FRP Reinforced Concrete Sections Subjected to Combined Axial and Bending Regime

Mattia Mairone [1,*], Gaetano Maragno [2], Davide Masera [2] and Mauro Corrado [1]

[1] Department of Structural, Geotechnical and Building Engineering (DISEG), Politecnico di Torino, 10129 Torino, Italy
[2] Masera Engineering Group S.r.l., Corso Bolzano 14, 10121 Turin, Italy
* Correspondence: mattia.mairone@polito.it

Abstract

Hybrid reinforced concrete (HRC) sections combining steel and fiber-reinforced polymer (FRP) bars provide a structural solution that balances durability, load-bearing capacity and energy dissipation. However, the absence of unified design provisions and the coexistence of distinct safety formats in European and American codes complicate the consistent assessment of ultimate limit state behavior under combined axial force and bending moment. In this study, a strain-based sectional model founded on compatibility and internal force equilibrium is implemented through a layer-by-layer numerical integration procedure to generate axial force–bending moment (N–M) interaction domains and moment–curvature (M–χ) relationships. The formulation is extended to a dimensionless framework in terms of normalized axial load, bending moment, total hybrid mechanical reinforcement ratio ω_h and hybridization parameter R. The analysis is conducted within two regulatory formats: the European framework based on Eurocode 2 and CNR-DT 203 R1/2026 and the American framework based on ACI 318-25 and ACI 440.11-22. The results show that increasing ω_h leads to a progressive expansion of the interaction domain and modifies the transition between FRP rupture-controlled and steel-yielding-controlled limit states. Increasing R shifts balanced conditions towards higher axial compression and bending levels. Differences between the two regulatory approaches are observed in terms of predicted curvature capacity and design resistance within the N–M domain, reflecting the distinct safety formats adopted. The proposed dimensionless parametric formulation enables consistent comparison of hybrid configurations and provides basis for interpreting failure-mode transitions and deformation capacity of HRC sections under combined axial and flexural actions.

Keywords: hybrid reinforcement; FRP bars; steel bars; reinforced concrete structures; moment curvature relationship; N–M interaction diagram; ductility; energy dissipation

Check for updates

Academic Editors: Dayou Luo and Kejin Wang

Received: 9 April 2026
Revised: 8 May 2026
Accepted: 9 May 2026
Published: 13 May 2026

Copyright: © 2026 by the authors. Licensee MDPI, Basel, Switzerland. This article is an open access article distributed under the terms and conditions of the Creative Commons Attribution (CC BY) license.

1. Introduction

The durability and structural reliability of reinforced concrete (RC) infrastructures are significantly affected by chloride-induced corrosion of steel reinforcement in aggressive environments. Progressive corrosion leads to cracking, spalling, reduction in cross-sectional area, and deterioration of bond, thereby shortening service life and increasing maintenance costs. Conventional mitigation strategies include the use of corrosion-protected or high-performance steel reinforcement; however, these solutions involve higher initial costs and do not fully eliminate long-term degradation mechanisms [1]. Fiber-reinforced

polymer (FRP) reinforcement has therefore emerged as an alternative solution for applications exposed to aggressive environments. FRP bars are characterized by inherent resistance to corrosion, high tensile strength, low density, and electromagnetic neutrality, and have been employed in structural applications for several decades [2,3]. Nevertheless, their linear-elastic brittle behavior and relatively low elastic modulus compared with steel impose limitations in terms of energy dissipation and deformation capacity, and serviceability performance.

The mechanical response of FRP–RC members differs substantially from that of conventional steel-reinforced members: steel exhibits ductile yielding and strain hardening, whereas FRP reinforcement remains linear elastic up to rupture. Therefore, steel–RC elements are typically governed by ultimate limit state (ULS) requirements, often resulting in conservative serviceability performance [4,5], whereas FRP–RC members are frequently governed by serviceability limit state (SLS) constraints, leading to overdesigned ultimate strength [6].

This asymmetry has motivated the development of hybrid reinforced concrete (HRC) sections combining steel and FRP reinforcements [7,8]. In such systems, steel contributes ductility and post-yield deformation capacity, whereas FRP reinforcement enhances durability, particularly when placed in the outermost layers or at corners exposed to aggressive environments [9]. Experimental investigations have confirmed that hybrid sections may provide improved stiffness and ductility compared with purely FRP-reinforced members [10], although reliable prediction of ductility activation mechanisms, failure-mode transitions and scalable design-oriented modeling frameworks remain an open research issue [11].

Most available studies on hybrid steel–FRP systems have focused on flexural members. Simplified design-oriented approaches have been proposed to facilitate the transformation of conventional steel–RC beams into hybrid configurations while maintaining the total number of longitudinal bars [12]. Reinforcement-ratio limits, hybrid stiffness indices and strain-based failure classifications have been introduced within ACI-based frameworks to ensure ductile flexural behavior and to predict ULS capacity [13,14]. Experimental evidence has demonstrated that the hybrid reinforcement ratio governs the strength–ductility trade-off, whereas reinforcement distribution influences stiffness and post-elastic response, particularly in continuous members [15–17]. In contrast, research on HRC columns remains comparatively limited, particularly with respect to compression behavior, ductility activation, and seismic response [18,19]. Nonlinear fiber-section approaches have been adopted to simulate moment–curvature response and failure mode (FM) evolution of hybrid members [20,21]. Recent experimental and numerical investigations on hybrid steel-GFRP reinforced concrete columns and frame systems have highlighted the influence of the steel-to-FRP replacement ratio on drift capacity, post-yield stability, energy dissipation and global seismic performance [22,23].

Despite these advances, no unified design framework establishes a consolidated baseline methodology for HRC elements under combined axial force and bending moment. In this context, dimensionless parametric approaches have been successfully adopted for steel-reinforced concrete sections [24,25]. However, their systematic extension to hybrid steel–FRP sections remains limited. In particular, balanced FM and their transitions across the axial force–bending moment interaction domain have not yet been consistently framed within a unified mechanics-based and code-comparative format.

The critical assessment of existing contributions reveals, therefore, three main limitations: (i) simplified design-oriented approaches are confined to pure flexure and do not address the combined N–M regime; (ii) nonlinear fiber-section models are applied to individual configurations without parametric generalization; (iii) dimensionless formula-

tions have been developed for steel–RC sections only. No previous study has combined a mechanics-based sectional model with a dimensionless parametric framework to systematically map failure-mode transitions for HRC sections across the full N–M interaction domain under two distinct normative formats.

The novelty of the present study lies in the development of a unified, mechanics-based, dimensionless parametric formulation to generate axial force vs. bending moment (N–M) interaction diagrams for HRC sections. This formulation introduces the total hybrid mechanical reinforcement ratio ω_h and the hybridization parameter R as governing variables. It enables the systematic identification of balanced failure mode transitions across the full N–M interaction domain.

In addition, the analysis extends the investigation to the moment–curvature (M–χ) analysis to quantify deformation capacity, curvature ductility and energy dissipation. The present investigation led to the construction of a structured dataset of ultimate limit state failure modes for varying axial force levels combined with different steel–FRP reinforcement ratios, providing a consistent basis for mapping failure mode domains and balanced transitions. The ULS FMs of the investigated sections are further validated through reinforcement area design diagrams expressed in terms of FRP and steel longitudinal reinforcement areas [26], consistent with the adopted parametric methodology.

Attention is devoted to the evaluation of ductility and energy dissipation capacity of HRC sections, which represents a fundamental property to control deformability and seismic design [27,28]. Classical curvature ductility indices, defined with respect to steel yielding, are meaningful only when steel governs the response. For FRP-dominated configurations, alternative deformation-based or energy-based measures have been proposed [29], while equivalent steel-section approaches have been introduced to establish lower and upper bounds for hybrid curvature capacity [13]. Previous analytical studies on hybrid strengthening and equivalent-section formulations have confirmed that curvature-based ductility metrics remain mechanically consistent when steel yielding precedes FRP rupture and concrete crushing governs the ultimate compressive limit [30]. Since moment–curvature response represents the basis for non-linear analysis of RC frame structures, its accurate prediction is essential for assessing strength, stiffness degradation, and hysteretic energy dissipation under cyclic loading.

2. Material Modeling

The structural design of RC members is governed by codified provisions that reflect the mechanical assumptions adopted for the constituent materials. When steel and FRP bars are used as longitudinal reinforcement, distinct regulatory approaches are required to represent their different constitutive behavior. For conventional steel-reinforced concrete, design rules are consolidated within comprehensive international standards, including EN 1992-1-1 (EC2) [31] in Europe and ACI 318-25 [32] in the United States. Additional standards are instead required for FRP reinforcement, such as, for instance, CNR-DT 203 R1/2026 [33] in Italy, ACI 440.11-22 [2] and AASHTO LRFD for GFRP 2018 [34] in the United States, and CSA S806-12 [35] in Canada, complemented by ASTM standards [36,37] defining material properties and testing procedures.

In the present study, these provisions are consistently adopted to compute the axial force–bending moment interaction diagrams of hybrid steel–FRP reinforced concrete sections within two regulatory formats. The comparison is driven by the different safety formats used to derive design resistance. European standards introduce partial safety factors at material level to account for uncertainties in material properties, modeling assumptions, and execution variability, thereby defining design material strengths and corresponding sectional resistances. In contrast, the American approach evaluates nominal sectional

capacity and subsequently applies a strain-dependent strength reduction factor (SRF) ϕ at sectional level to achieve the target reliability.

2.1. Concrete

The parabola–rectangle stress–strain relationship prescribed by Eurocode 2 for concrete is herein adopted:

$$\sigma_c = \begin{cases} f_{cd} \cdot \left[1 - \left(1 - \dfrac{\varepsilon_c}{\varepsilon_{c2}}\right)^2\right] & \text{if } 0 \le \varepsilon_c \le \varepsilon_{c2} \\ f_{cd} & \text{if } \varepsilon_{c2} \le \varepsilon_c \le \varepsilon_{cu} \end{cases} \quad (1)$$

where ε_{c2} is the strain at the peak compressive stress and ε_{cu} is the ultimate compressive strain, equal to 0.0035 for Eurocode 2 and 0.003 for ACI 318-25.

According to Eurocode 2, the design compressive strength of concrete is defined as:

$$f_{cd} = \alpha_{cc} \cdot \frac{f_{ck}}{\gamma_c} \quad (2)$$

where f_{ck} is the characteristic compression strength, the partial safety factor γ_c accounts for material variability and modeling uncertainty, and the coefficient α_{cc} considers long-term effects and unfavorable loading conditions. In practical design applications, α_{cc} is generally taken equal to 0.85. Within the American framework, the specified compressive strength f'_c is used directly as the reference concrete strength, without the application of partial safety factors at the material level. The tensile behavior of concrete is neglected in the ultimate limit state analysis.

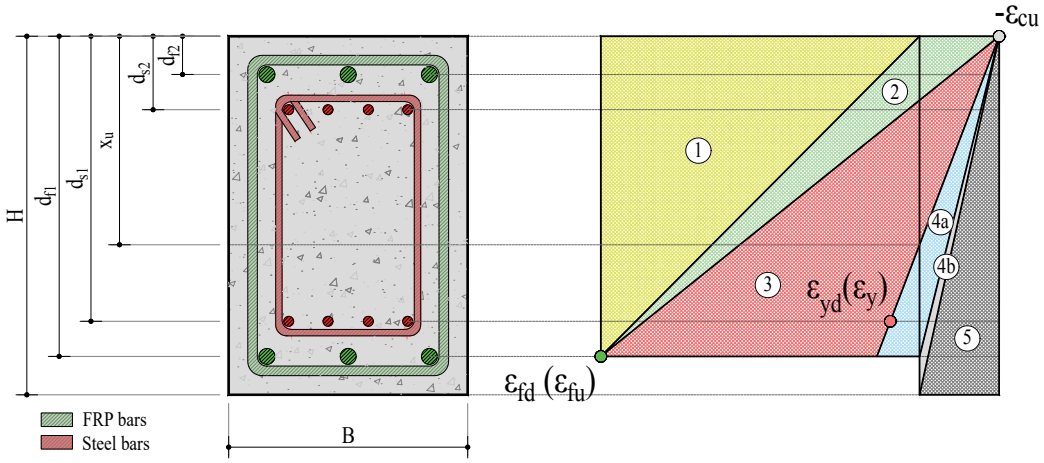
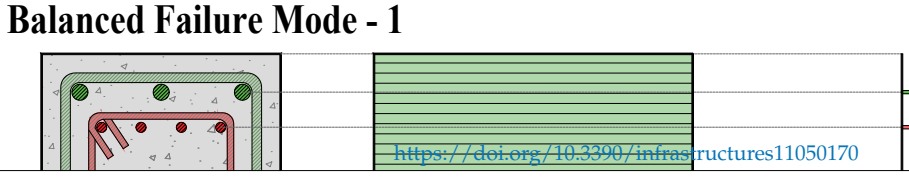


Figure 1. Arrangement of steel and FRP reinforcement within the cross section and failure modes for HRC sections.



https://doi.org/10.3390/infrastructures11050170

In this study, FRP bars are modeled in accordance with the European provisions (CNR-DT 203 R1/2026 [33]) and the American code requirements (ACI 440.11-22 [2]). In both approaches, FRP reinforcement is idealized as linear-elastic up to rupture; accordingly, bar stress is evaluated as $\sigma_{frp} = E_{frp} \cdot \varepsilon_{frp}$, with no yielding or post-peak capacity. Within the sectional analysis, the compressive contribution of FRP bars is conservatively neglected.

According to CNR-DT 203 R1/2026 [33], the design tensile strength of FRP bars is:

$$f_{fd} = \eta_T \cdot \eta_a \cdot \eta_{c,l} \cdot \frac{f_{fk}}{\gamma_f} \tag{3}$$

where f_{fk} is the characteristic tensile strength of the FRP bar, η_a denotes the environmental conversion factor, η_T the conversion factor accounting for temperature effects, and $\eta_{c,l}$ the conversion factor associated with long-term static fatigue. The parameter γ_f represents the partial safety factor for the FRP reinforcement.

According to ACI 440.11-22 [2], the guaranteed ultimate tensile strength is:

$$f_{fu} = C_E \cdot f^*_{fu} \tag{4}$$

where f^*_{fu} is the guaranteed tensile strength of the FRP bar and C_E denotes the environmental reduction factor taken equal to 0.85 for bars embedded in concrete.

3. Algorithm to Predict the Combined Axial Force–Bending Moment Response

This section presents the analytical model implemented in a Matlab script for predicting the axial force vs. bending moment resistance of HRC sections with internal steel reinforcement and external FRP bars, as illustrated in Figure 1. The sectional response is evaluated assuming a linear distribution of strain across the cross-section by invoking the Euler–Bernoulli hypothesis. In addition, the strain in the reinforcement, whether in tension or compression, is the same as that in the surrounding concrete (i.e., a perfect bond exists between reinforcements and concrete).

The salient failure modes adopted for the construction of the N–M interaction diagram are illustrated in Figure 1. They include:

- **Field 1:** The section remains entirely in tension, with the FRP reinforcement operating in its linear elastic range and the steel reinforcement potentially yielded in tension. The neutral axis migrates progressively toward the top chord while the top fiber strain decreases from the FRP rupture strain toward zero.
- **Field 2:** The compression zone develops and enlarges as the most compressed fiber strain increases from zero to ε_{cu}, while the bottom FRP layer is maintained at its rupture strain. The neutral axis migrates downward, transitioning the section from a cracked configuration toward the balanced failure condition BFM-2-3.
- **Field 3:** Concrete crushing is sustained at the top fiber ($\varepsilon_{top} = \varepsilon_{cu}$) while the bottom fiber strain decreases from ε_{fd} until the outermost steel layer attains ε_{sy} at BFM-3-4a. This field is associated with the peak flexural capacity of the section; beyond BFM-3-4a, further axial compression produces a monotonic reduction in bending resistance.
- **Field 4a:** Concrete crushing is sustained at the top fiber while the bottom fiber strain decreases from ε_{sy} toward zero. The neutral axis migrates downward until it coincides with the outermost FRP layer at BFM-4a-4b, where the FRP strain vanishes.
- **Field 4b:** All reinforcement layers operate under compressive strains and the bending moment decreases as axial compression dominates the sectional response.

- **Field 5:** Curvature diminishes to zero and the bending moment vanishes as the bottom fiber strain approaches ε_{cu}, yielding the concentric compression capacity governed by the combined resistance of concrete and steel reinforcement.

Each field is defined by prescribed boundary strain conditions at the extreme fibers and corresponding material limit states.

The extremes of the failure modes can be identified as Balanced Failure Modes (BFMs), characterized by the simultaneous attainment of specific material limit strains in concrete, steel, or FRP reinforcement. They represent mechanically meaningful boundary conditions within the sectional response. Figure 2 illustrates six of the seven BFM configurations adopted in the present study. For each case, the section layout, the corresponding linear strain distribution, and the associated stress distribution in concrete, steel, and FRP reinforcement are shown.

Table 1 provides a synthetic overview of the failure modes and balanced failure mode transitions illustrated in Figure 1. For each configuration, the governing strain conditions at the top and bottom fibers, the controlling material at ultimate limit state, and the corresponding region within the N–M interaction domain are reported.

Table 1. Summary of failure modes: governing strain conditions, controlling material and position within the N–M domain.

Failure Mode	Top Fiber Strain	Bottom Fiber Strain	Controlling Material	N–M Domain Region
FM-1	$\varepsilon_c > 0$ (tension)	$\varepsilon_f = \varepsilon_{fd}$	FRP rupture	Pure tension
BFM-1-2	$\varepsilon_c = 0$	$\varepsilon_f = \varepsilon_{fd}$	FRP rupture	Tension boundary
FM-2	$0 > \varepsilon_c > -\varepsilon_{cu}$	$\varepsilon_f = \varepsilon_{fd}$	FRP rupture	Tension-controlled
BFM-2-3	$\varepsilon_c = -\varepsilon_{cu}$	$\varepsilon_f = \varepsilon_{fd}$	Simultaneous FRP rupture and concrete crushing	Balanced transition
FM-3	$\varepsilon_c = -\varepsilon_{cu}$	$\varepsilon_{sy} < \varepsilon_f < \varepsilon_{fd}$	Concrete crushing with steel yielded	Transition region
BFM-3-4a	$\varepsilon_c = -\varepsilon_{cu}$	$\varepsilon_s = \varepsilon_{sy}$	Simultaneous concrete crushing and steel yielding	Balanced transition
FM-4a	$\varepsilon_c = -\varepsilon_{cu}$	$0 < \varepsilon_s < \varepsilon_{sy}$	Concrete crushing with steel elastic	Compression-controlled
BFM-4a-4b	$\varepsilon_c = -\varepsilon_{cu}$	$\varepsilon_f = 0$	Concrete crushing	Compression boundary
FM-4b	$\varepsilon_c = -\varepsilon_{cu}$	$\varepsilon_f < 0$ (compression)	Concrete crushing	Compression-controlled
BFM-4b-5	$\varepsilon_c = -\varepsilon_{cu}$	$\varepsilon_f \to -\varepsilon_{cu}$	Full section approaching crushing	Compression boundary
FM-5	$\varepsilon_c = -\varepsilon_{cu}$	$\varepsilon_f = -\varepsilon_{cu}$	Uniform concrete crushing	Pure compression

The layer-by-layer numerical integration (LLNI) method was used to compute interaction diagrams and moment–curvature relationships. The concrete cross-section is discretized into N_{St} horizontal strips of constant thickness, as schematically illustrated in Figure 3. The axial strain of the ith concrete layer is evaluated at its centroid as a linear function of the neutral axis depth x, based on strain compatibility between the layer position and the concrete strain at the extreme compressed fiber, ε_c. The value of ε_c may be lower than the ultimate compressive strain ε_{cu}, depending on the governing strain state. The concrete stress within each strip is assumed constant and is evaluated using the selected constitutive relationship at the strip centroid strain.

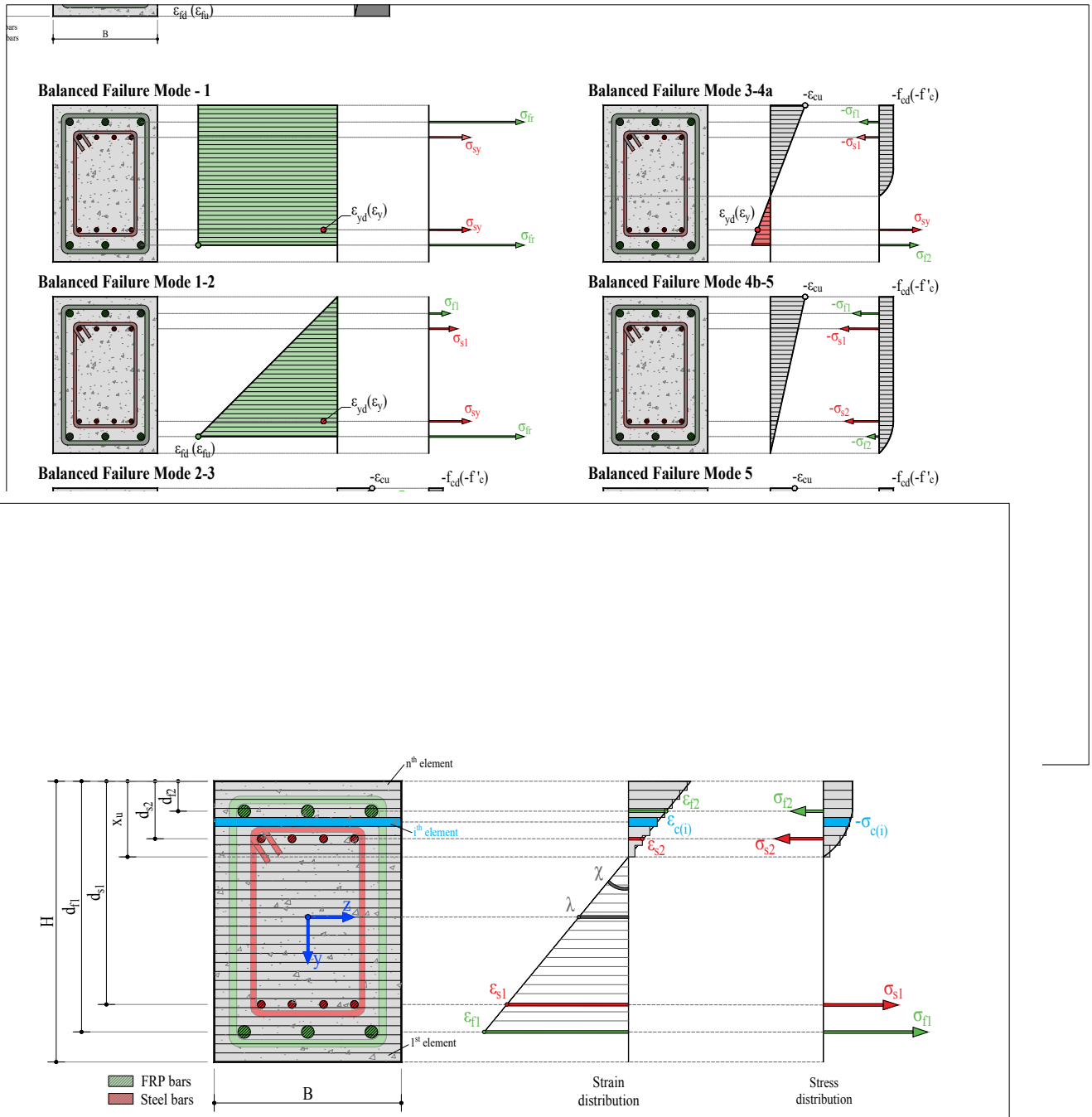


Figure 3. Cross-section, strain and stress distributions for the layer-by-layer numerical integration method.

3.1. Salient Points on the N–M Interaction Diagram

In this section, the equations implemented within the LLNI method to evaluate the design axial force and bending moment for the different failure regions and balanced failure modes are reported. For the sake of conciseness, only the equations pertaining to the European framework (Eurocode 2 + CNR) are reported. However, they are valid also for the ACI framework upon the following modifications:

- the design compressive strength of concrete f_{cd} is replaced by the specified compressive strength f'_c;
- the design yield strength of steel f_{yd} is replaced by the nominal yield strength f_y.

All the equations are expressed in general form: stress resultants and axial force terms are assigned their algebraic sign according to the adopted sign convention (i.e., tensile quantities are positive and compressive quantities are negative).

Equations (5) represent the general expressions for the design axial force (5a) and the design bending moment (5b), valid for all failure modes, with the stress and strain quantities evaluated at the corresponding limit states.

$$N_{Rd} = \sum_{i}^{N_{st}} \sigma_{cd}(i) \cdot b_{st}(i) \cdot h_{st}(i) + \sum_{i}^{N_s} \varepsilon_{syd}(i) \cdot E_s(i) \cdot A_s(i) + \sum_{i}^{N_f} \varepsilon_{fd}(i) \cdot E_f(i) \cdot A_f(i) \quad (5a)$$

$$M_{Rd} = \sum_{i}^{N_{st}} N_{cd}(i) \cdot (y_{st}(i) - y_{G,o}) + \sum_{i}^{N_s} N_{sd}(i) \cdot (d_s(i) - y_{G,o}) + \sum_{i}^{N_f} N_{fd}(i) \cdot \left(d_f(i) - y_{G,o}\right) \quad (5b)$$

It is worth noting that, when applied within the ACI context, Equations (5) provide the nominal axial and bending moment capacities. The design values are then obtained by applying the Strength Reduction Factor (SRF), as detailed in Section 3.2.

BFM-5 represents pure axial compression load with no bending moments. The design axial compression load can be calculated using Equation (6) where the contribution of the FRP bars is partially considered by assuming that they have the same strength and stiffness as the surrounding concrete.

$$N_{Rd} = f_{cd} \cdot \left(\sum_{i}^{N_{st}} b_{st}(i) \cdot h_{st}(i) - \sum_{i=1}^{N_s} A_{s,i} \right) + \sum_{i=1}^{N_s} f_{syd}(i) \cdot A_s(i) \quad (6)$$

BFM-4b-5 represents the condition of the neutral axis located at the least compressed edge while maintaining the maximum concrete compressive strain at the most compressed edge.

BFM-4a-4b represents the condition where the neutral axis coincides with the FRP bars at the lowest level, while the most compressed fiber attains the ultimate concrete compressive strain ε_{cu}.

BFM-3-4a corresponds to a neutral-axis configuration in which the most compressed concrete fiber reaches the crushing strain limit while the outermost steel reinforcement layer reaches the steel yielding strain. The corresponding neutral axis depth $x_{u,3-4a}$ is obtained from strain compatibility:

$$x_{u,3-4a} = \frac{|\varepsilon_{cu}|}{|\varepsilon_{cu}| + \varepsilon_{syd}} \cdot d_{s,1} \quad (7)$$

The equilibrium between the internal force resultants and the applied external forces is expressed by Equation (8):

$$\sum_{k=1}^{N_{st}} \sigma_{c,k} \cdot b_k \cdot h_k + A_{s1} \cdot f_{yd,1} + \sum_{i=2}^{N_S} A_{s,i} \cdot \sigma_{s,i} + \sum_{j=1}^{N_F} A_{f,j} \cdot \sigma_{f,j} = N_{Ed} \quad (8)$$

In this formulation, $A_{s,1}$ refers to the outermost tensile steel layer (layer-1), which has reached the yielding strain ε_{sy}, while the summation from $i = 2$ to N_S accounts for all remaining steel layers, which may or may not have yielded depending on their position relative to the neutral axis.

For a given applied axial load, the amount of reinforcement, both steel and FRP, that provides the condition of BFM-3-4a can be computed through Equation (9), obtained by rearranging Equation (8):

$$A_{s1} \cdot f_{yd,1} + \sum_{i=2}^{N_S} A_{s,i} \cdot \sigma_{s,i} + \sum_{j=1}^{N_F} A_{f,j} \cdot \sigma_{f,j} = N_{Ed} - \sum_{k=1}^{N_{st}} \sigma_{c,k} \cdot b_k \cdot h_k \quad (9)$$

The reinforcement amount required to satisfy this condition is frequently incompatible with the adopted cross-sectional dimensions and with the detailing provisions prescribed by current design standards [38]. Such a configuration may only be attained under high axial compression levels and is generally associated with brittle failure mechanisms [13].

In the hypothesis of steel reinforcement only, the tensile steel rebar area satisfying Equation (9), $A_{s,3-4a}$, is obtained by setting the contribution of the tensile FRP reinforcement to zero; the ordinate of the diagram in Figure 4 is thus obtained.

$$A_{s,3-4a} = \frac{N_{Ed} - \sum_{k=1}^{N_{st}} \sigma_{c,k} \cdot b_k \cdot h_k - \sum_{i=1}^{N_S} A_{s,i} \cdot \sigma_{s,i}^{(compressed)}}{f_{yd,1}} = A_{s1} + \sum_{i=2}^{N_S} \frac{A_{s,i} \cdot \sigma_{s,i}}{f_{yd,1}} \quad (10)$$

Under the same equilibrium framework, elimination of the tensile area of steel yields the abscissa of the diagram in Figure 4, corresponding to the FRP reinforcement area leading to the BFM-3-4a condition in the absence of tensile steel reinforcement:

$$A_{f,3-4a} = \frac{N_{Ed} - \sum_{k=1}^{N_{st}} \sigma_{c,k} \cdot b_k \cdot h_k - \sum_{i=1}^{N_S} A_{s,i} \cdot \sigma_{s,i}^{(compressed)}}{\sigma_{f,1}} = \sum_{j=1}^{N_F} \frac{A_{f,j} \cdot \sigma_{f,j}}{\sigma_{f,1}} \quad (11)$$

where $\sigma_{f,1}$ represents the stress in the outermost FRP layer, evaluated at a level lower than its rupture strength.

BFM-2-3 corresponds to a neutral-axis configuration in which the most compressed concrete fiber reaches the crushing strain limit while the outermost FRP layer simultaneously attains its rupture strain, with the outermost steel layer already yielded. The corresponding neutral-axis depth $x_{u,2-3}$ is obtained from strain compatibility:

$$x_{u,2-3} = \frac{|\varepsilon_{cu}|}{|\varepsilon_{cu}| + \varepsilon_{fd}} \cdot d_{f,1} \quad (12)$$

The equilibrium between the resultant of the internal forces and the applied axial load is expressed by Equation (13).

$$\sum_{k=1}^{N_{st}} \sigma_{c,k} \cdot b_k \cdot h_k + \sum_{i=1}^{N_S} A_{s,i} \cdot \sigma_{s,i} + A_{f1} \cdot f_{fd,1} + \sum_{j=2}^{N_F} A_{f,j} \cdot \sigma_{f,j} = N_{Ed} \quad (13)$$

For a given applied axial load, the total amount of reinforcement corresponding to the condition of BFM-2-3 is provided by Equation (14), obtained by rearranging Equation (13):

$$\sum_{i=1}^{N_S} A_{s,i} \cdot \sigma_{s,i} + A_{f1} \cdot f_{fd,1} + \sum_{j=2}^{N_F} A_{f,j} \cdot \sigma_{f,j} = N_{Ed} - \sum_{k=1}^{N_{st}} \sigma_{c,k} \cdot b_k \cdot h_k \quad (14)$$

In the hypothesis of steel reinforcement only, the total rebar area satisfying Equation (14), $A_{s,2-3}$, is obtained by setting the contribution of the FRP reinforcement to zero; the ordinate of the diagram in Figure 4 is thus obtained.

$$A_{s,2-3} = \frac{N_{Ed} - \sum_{k=1}^{N_{st}} \sigma_{c,k} \cdot b_k \cdot h_k - \sum_{i=1}^{N_S} A_{s,i} \cdot \sigma_{s,i}^{(compressed)}}{f_{yd,1}} = A_{s1} + \sum_{i=2}^{N_S} \frac{A_{s,i} \cdot \sigma_{s,i}}{f_{yd,1}} \quad (15)$$

Similarly, neglecting the summation terms associated with tensile steel reinforcement, the abscissa of the diagram in Figure 4 is obtained.

$$A_{f,2-3} = \frac{N_{Ed} - \sum_{k=1}^{N_{st}} \sigma_{c,k} \cdot b_k \cdot h_k - \sum_{i=1}^{N_S} A_{s,i} \cdot \sigma_{s,i}^{(compressed)}}{f_{fd,1}} = A_{f1} + \sum_{j=2}^{N_F} \frac{A_{f,j} \cdot \sigma_{f,j}}{f_{fd,1}} \quad (16)$$

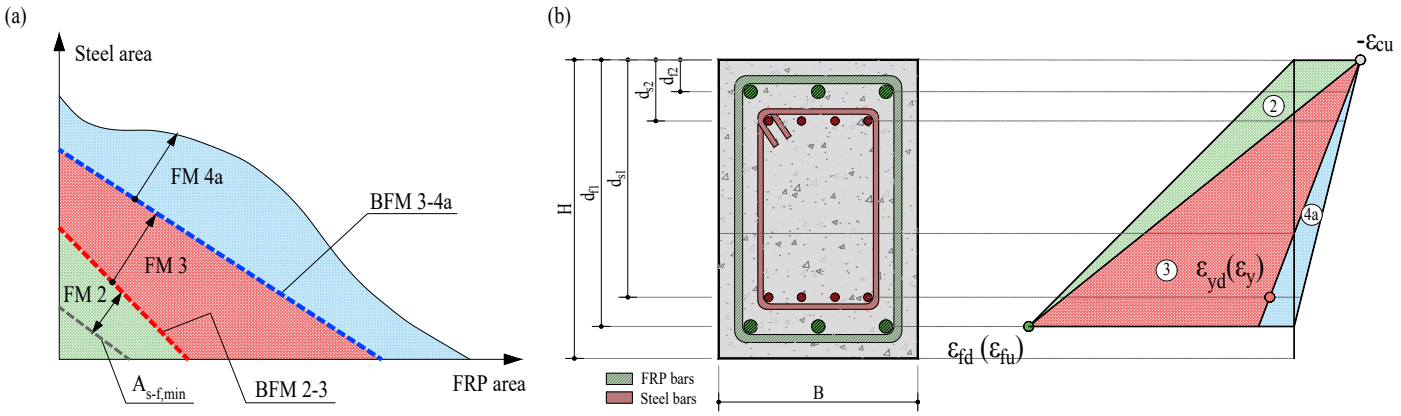


Figure 4. (**a**) Failure mode regions in the tensile reinforcement plane A_s–A_f and (**b**) HRC cross-section with ULS strain distributions for most typical failure modes.

3.2. ACI Framework

The application of Equations (5) to the ACI framework provides the nominal value of the resistant axial force and bending moment. Design values are then obtained by applying the SRF ϕ.

For members reinforced exclusively with steel bars, ACI 318-25 prescribes $\phi = 0.90$ when the net tensile strain in the extreme steel layer at nominal strength is at least 0.005, corresponding to the tension-controlled classification. For compression-controlled sections, the prescribed value is $\phi = 0.65$. A linear transition applies between the two limits as a function of the net tensile strain at the extreme tension reinforcement. The higher value assigned to tension-controlled behavior reflects the ductile nature of steel yielding, which provides energy dissipation and warning of impending failure.

For members reinforced exclusively with GFRP bars, ACI 440.11-22 adopts a different SRF format. The tension-controlled limit is set at $\phi = 0.55$, reflecting the brittle nature of FRP rupture at ultimate conditions. The compression-controlled limit is $\phi = 0.65$. A linear transition applies between the two thresholds. This represents the opposite trend with respect to ACI 318-25. The inversion reflects the fundamentally different failure characteristics of the two reinforcement types. FRP rupture is sudden and provides no warning. Compression-controlled failure in GFRP–RC sections involves concrete crushing, which is comparatively less brittle and exhibits larger deformations prior to collapse. This justifies the higher SRF value assigned to the compression-controlled regime.

For steel–RC members strengthened with externally bonded FRP systems, ACI 440.2R-17 introduces an additional material reduction factor $\psi_f = 0.85$, applied to the FRP contribution prior to the global SRF ϕ. This factor accounts for the additional uncertainty associated with FRP material properties, manufacturing variability and bond behavior, and is independent of the strain-dependent ϕ factor applied at the sectional level.

No specific SRF provisions are currently codified for HRC sections combining internal steel and internal FRP longitudinal bars. When the steel reinforcement in an HRC section satisfies the tension-controlled threshold ($\varepsilon_s \geq 0.005$), the adoption of $\phi = 0.90$ from ACI 318-25 remains mechanically consistent with the ductility-based rationale of the code, as proposed by Hussain et al. [39]. However, HRC members may reach ultimate conditions with steel strains exceeding yield by approximately 0.003 while FRP simulta-

neously approaches rupture. Although the steel formally satisfies the tension-controlled threshold, the ULS is partially governed by the brittle FRP response. Reliability-based investigations indicate that a reduction in the SRF below 0.90 is recommended in such cases [14,40]. For instance, Tarawneh et al. [41] found that $\phi = 0.80$ provides reliability levels consistent with design targets for hybrid sections.

In the present study, a different approach is applied, in which the additional uncertainty introduced by FRP reinforcement is explicitly addressed through a dedicated material reduction factor $\psi_f = 0.85$, applied to the FRP contribution prior to SRF. This two-factor format separates FRP material variability from the global ductility-based factor, extending to internal hybrid reinforcement the concept introduced by ACI 440.2R-17 for externally bonded systems. Accordingly, $\phi = 0.90$ is retained, consistent with the tension-controlled classification of ACI 318-25, since the FRP-related uncertainty is independently captured by ψ_f. The nominal flexural strength of HRC sections is thus computed by multiplying the FRP contribution by $\psi_f = 0.85$ and subsequently applying $\phi = 0.90$, acknowledging that this extension represents an approximation pending code provisions specifically calibrated for HRC structural elements.

In addition to the application of the SRF, the compressive branch of the *N*–*M* interaction domain is limited by a maximum nominal axial strength, N_{max}, computed with the following expressions:

$$N_{max} = 0.8 \cdot \left[0.85 \cdot f'_c \cdot (A_g - A_s) + f_y \cdot A_s\right] \quad (17)$$

according to ACI 318-25.

For HRC sections subjected to combined axial compression and bending, the FRP bars located on the tensile side of the neutral axis may develop tensile strains despite the overall compressive loading state. When the design axial load exceeds 10% of the gross concrete capacity (i.e., $N_{Ed} > 0.10 \cdot f'_c \cdot A_g$), the tensile strain in the FRP longitudinal bars is limited to 0.01, since mobilizing the full tensile capacity of FRP may exceed 2%, leading to excessive and structurally unacceptable column curvature. Accordingly, within the proposed LLNI equilibrium procedure, the design tensile strength of FRP bars is taken as the lesser of the design rupture strength f_{fu} and the stress corresponding to the strain limit, i.e., $f_f = \min(f_{fu}, E_f \cdot 0.01)$, and this capped value is used in the force and moment resultant calculations. The compressive contribution of FRP reinforcement is neglected and the compression zone is treated as plain concrete, in accordance with current ACI-based provisions. While experimental investigations report compressive-to-tensile strength ratios in the range 0.6–0.9 and compressive modulus values approaching the tensile modulus [42,43], substantial variability attributed to slenderness effects, boundary conditions, and micro-fiber buckling precludes the definition of standardized compressive material properties [44]. It is acknowledged that this conservative assumption may result in an underestimation of the actual load-carrying capacity of compression members [45].

3.3. Numerical Procedure for N–M Interaction Diagram

The *N*–*M* interaction diagram is constructed using a direct strain-controlled approach that directly prescribes limit strain states at critical section fibers, thereby avoiding iterative equilibrium searches. The BFMs corresponding to the transition between adjacent strain fields are schematically illustrated in Figure 1. Under the assumption that plane sections remain plane, the longitudinal strain field across the section depth is fully described by two kinematic parameters: the axial strain at the centroid of the section, λ, and the curvature, χ. The strain at an arbitrary vertical coordinate y is expressed as:

$$\varepsilon(y) = \lambda + \chi \cdot (y - y_{G,o}) \quad (18)$$

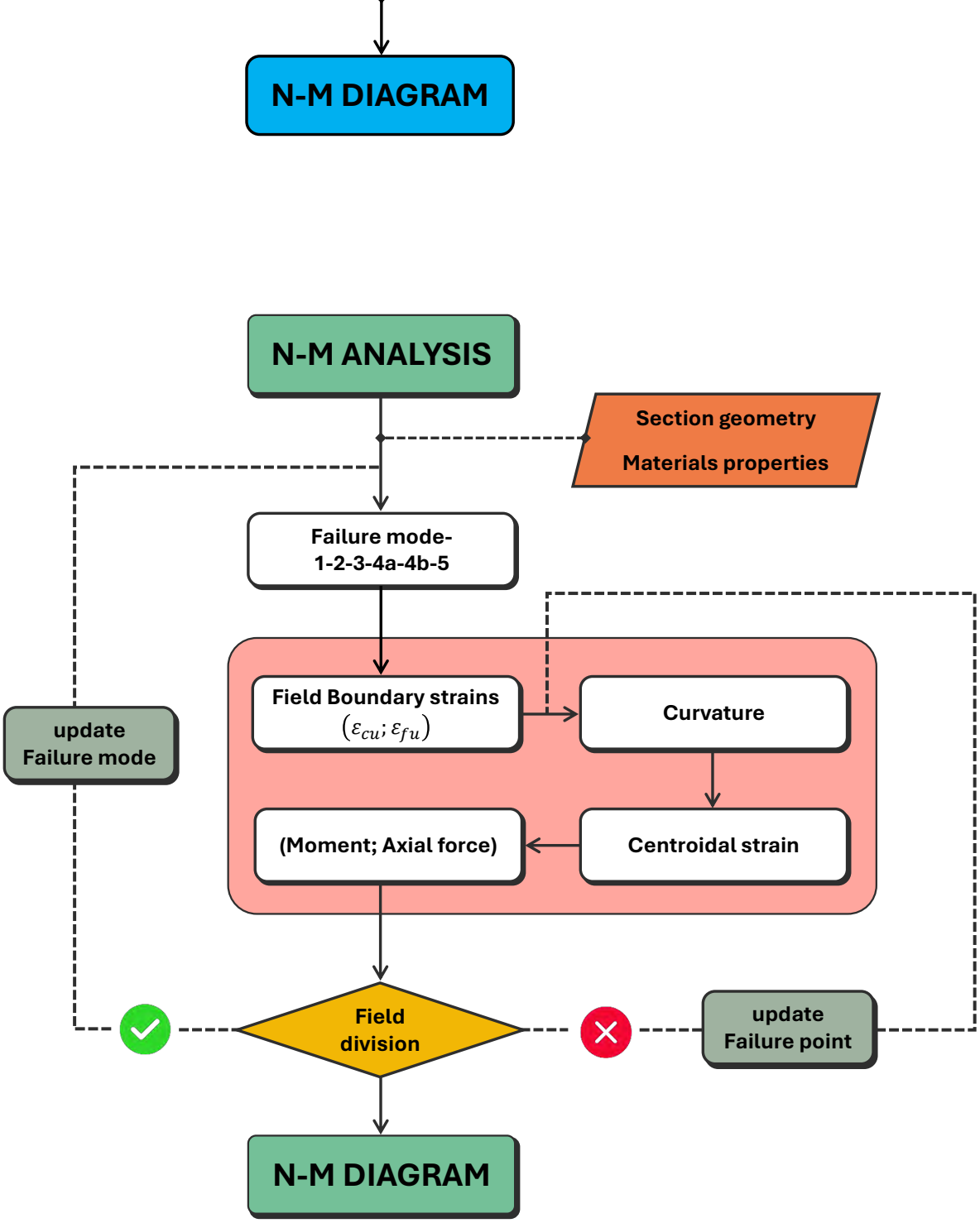


Figure 5. *N–M* interaction domain algorithm workflow.

The interaction domain is decomposed into the six distinct strain Fields 1-2-3-4a-4b-5. For each field, a boundary strain parameter is varied linearly over a predefined number of discretization points, while the complementary fiber strain is governed by the corresponding failure condition. Sectional force resultants are evaluated through the LLNI method.

3.4. Numerical Procedure for Moment–Curvature Relationship

The moment–curvature relationship is constructed under prescribed constant axial force N_{Ed}, with curvature χ as the independent variable. The longitudinal strain distribution follows plane-section kinematics in accordance with Equation (18). The analysis proceeds in two sequential phases: determination of the admissible curvature range $[\chi_{min}, \chi_{max}]$, followed by iterative construction of the M–χ diagram over that range, as illustrated in Figure 6.

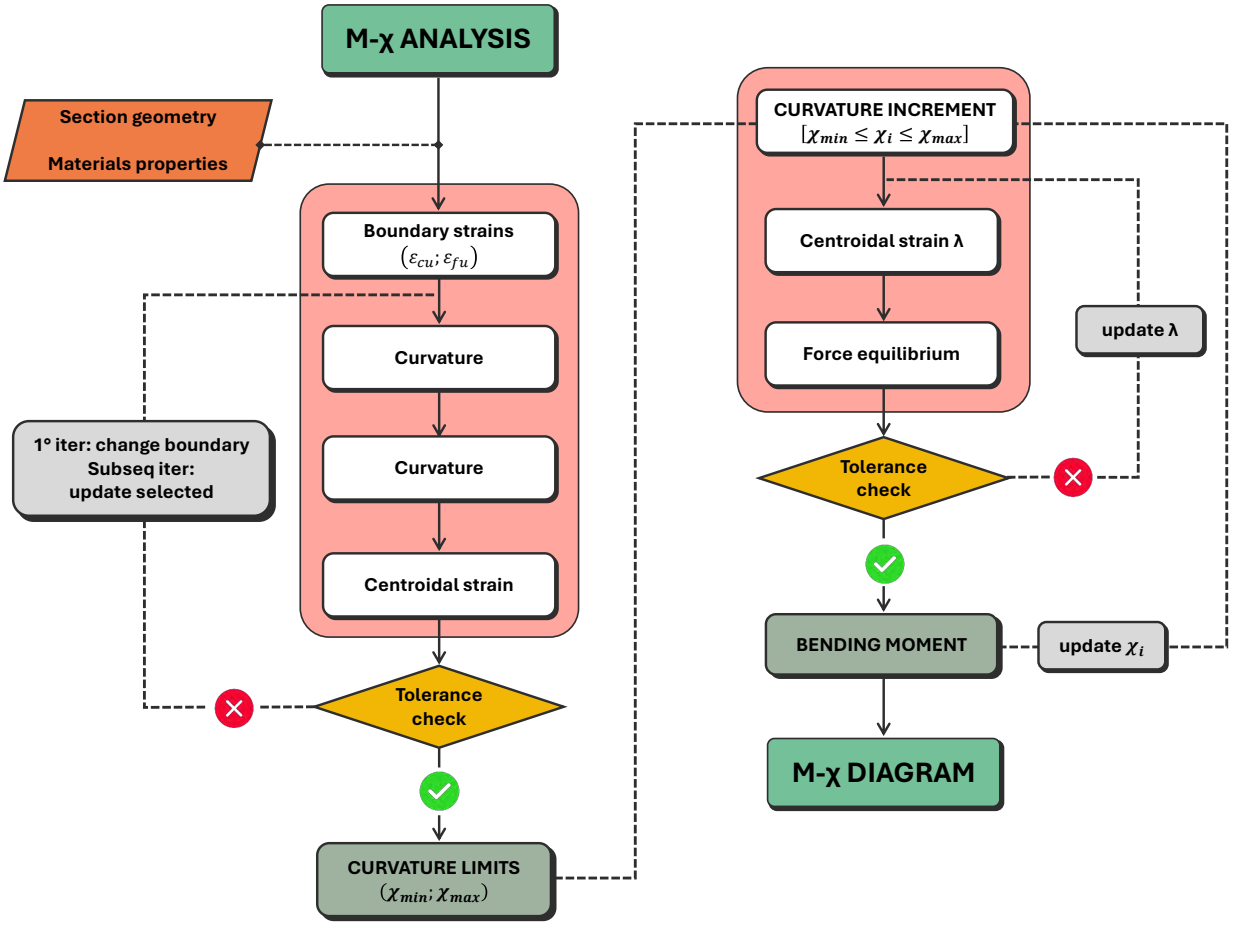


Figure 6. Moment–curvature algorithm workflow.

- **Curvature Limits**

  The limit curvatures bounding the range of admissible response are established separately for positive and negative bending. For each sign of curvature, the extreme compressed concrete fiber is fixed at the ultimate compressive strain ε_{cu}, while the opposite (tensioned) boundary strain is treated as the single free variable and initialized at the FRP design ultimate strain ε_{fd} as a starting estimate. An iterative correction scheme then adjusts the tensioned-boundary strain until axial equilibrium with the target force N_{Ed} is satisfied. At each iteration, the sign of the axial-force residual determines the direction of the correction: the tensioned-fiber strain is increased when $N < N_{Ed}$ (insufficient compression) and decreased when $N > N_{Ed}$ (excess compression). The strain increment is computed under the assumption of a locally linear axial response governed by the secant concrete modulus at peak stress:

$$\Delta\varepsilon = \frac{\left| N(\chi^{(k)}) - N_{Ed} \right|}{\left| \frac{f_{cd}}{\varepsilon_{c2}} \right| \cdot A_g} \tag{19}$$

  where $\chi^{(k)}$ is the trial curvature at iteration k, f_{cd} is the concrete compressive strength, ε_{c2} is the strain at peak stress (not the ultimate strain ε_{cu}), and A_g is the gross cross-sectional area. The curvature is updated at each step as:

$$\chi^{(k)} = \frac{\varepsilon_t^{(k)} - \varepsilon_{cu}}{d_{ref}} \tag{20}$$

where $\varepsilon_t^{(k)}$ is the current tensioned-boundary strain and d_{ref} is the distance from the compressed fiber to the extreme reinforcement layer. Convergence is declared when:

$$\left|N(\chi^{(k)}) - N_{Ed}\right| < \tau_\chi = \frac{|f_{cd}| \cdot A_g}{1000} \tag{21}$$

The converged curvatures χ_{max} (positive bending) and χ_{min} (negative bending) define the sweep range for the moment–curvature diagram.

- **Moment–Curvature Construction**

  At each curvature level χ_i, the centroidal strain λ, which at fixed curvature rigidly shifts the strain profile of Equation (18) along the section depth and thereby controls the resultant axial force, is treated as a free variable and adjusted iteratively to enforce $N = N_{Ed}$. The centroidal strain update is given by:

$$\Delta\lambda = \frac{N(i) - N_{Ed}}{\left|\frac{f_{cd}}{\varepsilon_{c2}}\right| \cdot A_g} \tag{22}$$

  To prevent numerical overshooting in the vicinity of material limit states, where constitutive nonlinearities are most pronounced, the correction is scaled by a relaxation factor: a more conservative value is applied when $|\chi|$ increases, since this drives the section toward concrete crushing where the response is highly nonlinear, while a less restrictive value is used when $|\chi|$ decreases, as the resulting tensile-dominated strain state yields a more stable iterative response. Convergence is declared when $|N_{Ed} - N| \leq$ tol. Upon convergence, the resulting bending moment is recorded and the procedure advances to the next increment. The complete M–χ relationship is thereby assembled continuously from the uncracked elastic regime through the ultimate limit state, governed by concrete crushing, steel yielding, or FRP rupture depending on the controlling failure mode.

4. Verification of the Proposed Model

The reliability of the proposed sectional model is assessed through a systematic comparison with experimental results available in the literature, focusing on two response quantities of primary structural significance: the yielding moment and the ultimate moment.

4.1. Experimental Database

A comprehensive benchmark database is compiled from the literature, collecting 93 HRC beams drawn from 18 independent experimental campaigns. All specimens are simply supported beams reaching failure in flexure, with no governing shear or bond mechanisms reported in the original sources. All specimens combine longitudinal steel and FRP reinforcement. The geometric and mechanical properties of all specimens are reported in Table A1 (Appendix A).

The collected database covers a wide range of governing parameters, as summarized in Table 2. The geometric parameters include the cross-section width b, the total depth h, the total beam span L_{tot}, and the shear span L_v. The reinforcement layout is described by the tensile steel area A_s, the tensile FRP area A_f, and the compressive steel area A'_s. The distances y_s and y_f denote the position of the centroid of the steel and FRP tensile reinforcement layers measured from the nearest tensile edge of the cross-section, respectively. The distance y'_s denotes the position of the centroid of the compressive steel layer measured from the nearest compressive edge. The mechanical properties include the concrete compressive strength f'_c, the steel yield strength f_y, the FRP ultimate tensile strength

f_{fu}, and the FRP tensile modulus of elasticity E_f. Distributional symmetry is classified according to the absolute value of skewness [46]: $|\gamma_1| < 0.5$ approximately symmetric, $0.5 \leq |\gamma_1| < 1.0$ moderately skewed, $|\gamma_1| \geq 1.0$ highly skewed. Kurtosis values refer to excess kurtosis (Fisher's definition). A similar statistical characterization of experimental databases for FRP-concrete systems can be found in [47,48].

Table 2. Descriptive statistics of the experimental database input parameters.

Parameter	Mean	Std. Deviation	CoV	Min	Median	Max	Skewness	Kurtosis
b [mm]	188	55.6	0.30	100	180	400	1.71	5.07
h [mm]	271	50	0.18	200	250	400	0.64	0.56
L_{tot} [mm]	2619	861	0.33	1350	2500	4600	0.62	−0.62
L_v [mm]	923	374	0.41	458	850	2100	1.03	1.24
A_s [mm^2]	291.5	211.6	0.73	78.5	226.2	981.7	1.82	2.90
A_f [mm^2]	231.6	151.7	0.65	28.0	226.2	981.7	1.76	5.60
A'_s [mm^2]	130.7	41.2	0.31	28.3	142.0	253.4	0.24	1.40
y_s [mm]	46.6	15.9	0.34	25.0	40.0	90.0	1.46	1.36
y_f [mm]	37.0	8.6	0.23	15.0	35.0	55.0	−0.17	0.56
f'_c [MPa]	36.9	11.3	0.31	20.0	34.0	75.9	1.25	2.08
f_y [MPa]	467.5	60.4	0.13	336.0	470.0	597.0	−0.82	−0.12
f_{fu} [MPa]	1144.6	627.5	0.55	449.0	956.4	2850.0	1.64	1.91
E_f [GPa]	62.1	38.0	0.61	35.0	46.0	165.0	1.92	2.20

The geometric parameters span a representative range of laboratory-scale specimens. The cross-section width b (mean 188 mm, CoV = 0.30) is highly positively skewed ($\gamma_1 = 1.71$, excess kurtosis 5.07), indicating a concentration in the lower range with few wider sections up to 400 mm. The depth h (mean 271 mm, CoV = 0.18) and total span L_{tot} show moderate positive skewness, consistent with the prevalence of laboratory-scale testing. The shear span L_v ($\gamma_1 = 1.03$) is highly positively skewed, reflecting a concentration of shorter shear spans with few specimens exceeding 1500 mm.

Among the mechanical properties, f_y is the least dispersed parameter (CoV = 0.13), with a moderately left-skewed distribution ($\gamma_1 = -0.82$) and near-zero excess kurtosis. The FRP tensile strength f_{fu} (mean 1144.6 MPa, CoV = 0.55) and modulus E_f (mean 62.1 GPa, CoV = 0.61) both exhibit highly right-skewed distributions, reflecting the predominance of low-modulus GFRP with a smaller subset of carbon or aramid fiber specimens in the upper tail. The concrete compressive strength f'_c ranges from 20.0 to 75.9 MPa (mean 36.9 MPa), with a highly positively skewed distribution ($\gamma_1 = 1.25$) produced by a subset of higher-strength specimens.

The reinforcement areas A_s and A_f are both highly right-skewed (skewness 1.82 and 1.76, excess kurtosis 2.90 and 5.60), with the higher kurtosis of A_f indicating a sharper peak and heavier right tail. The compression area A'_s is approximately symmetric (skewness 0.24), reflecting standardised compression detailing. The cover distance y_s (mean 46.6 mm) is highly positively skewed ($\gamma_1 = 1.46$), while y_f (mean 37.0 mm) is approximately symmetric ($\gamma_1 = -0.17$). The lower mean FRP cover confirms the typical HRC layout, consistent with the practice of placing corrosion-resistant reinforcement in the outermost layers.

The composition of the database in terms of FRP type, failure mode, and bar position is reported in Table 3. GFRP accounts for 61.29% of the specimens, followed by CFRP (17.20%), BFRP (16.13%), and AFRP (5.38%).

FM-3 (steel yielding followed by concrete crushing) dominates with 97.85% of specimens. FM-2 (FRP rupture with steel yielded) accounts for 2.15%. Regarding bar position, 52.69% of specimens have FRP and steel at the same level, while 45.16% feature external

FRP. Only 2.15% adopt external steel. The database is not perfectly balanced across all parameters. GFRP and FM-3 are over-represented. This reflects the actual distribution of available experimental data rather than a selection bias. The substantial size and heterogeneity of the 18 source campaigns mitigate the influence of any single program on the validation statistics.

Table 3. Distribution of FRP type, failure mode (FM), and bar position in the experimental database.

FRP Type	Count	FM	Count	Bar Position	Count
GFRP	57 (61.29%)	FM-3	91 (97.85%)	FRP and steel same level	49 (52.69%)
BFRP	15 (16.13%)	FM-2	2 (2.15%)	External FRP	42 (45.16%)
CFRP	16 (17.2%)			External steel	2 (2.15%)
AFRP	5 (5.38%)				

4.2. Validation Results

The numerical yielding and ultimate moments are computed for each of the 93 specimens using mean material properties as input. No partial safety factors or strength reduction factors are applied. The specimen-by-specimen comparison is provided in Table A2 (Appendix B).

The results are reported in Table 4 and visualized in Figures 7 and 8.

Table 4. Descriptive statistics of experimental and numerical yielding and ultimate moments.

Parameter	Mean	Std. Deviation	Skewness	Kurtosis	R^2
$M_{y,e}$ [kNm]	39.21	33.042	2.39	6.67	0.9885
$M_{y,num}$ [kNm]	38.24	32.491	2.56	7.39	
$M_{u,e}$ [kNm]	62.41	40.580	2.43	7.89	0.9887
$M_{u,num}$ [kNm]	62.02	40.803	2.37	7.28	

For the yielding moment, the mean numerical-to-experimental ratio is 0.978 with R^2 = 0.9885. The systematic underestimation is consistent with the adoption of an elastic–perfectly plastic constitutive law for steel, which neglects strain hardening at the yield transition.

For the ultimate moment, the mean ratio is 0.992 with R^2 = 0.9887. The close agreement confirms that the model does not exhibit a statistically significant bias at the 95% confidence level.

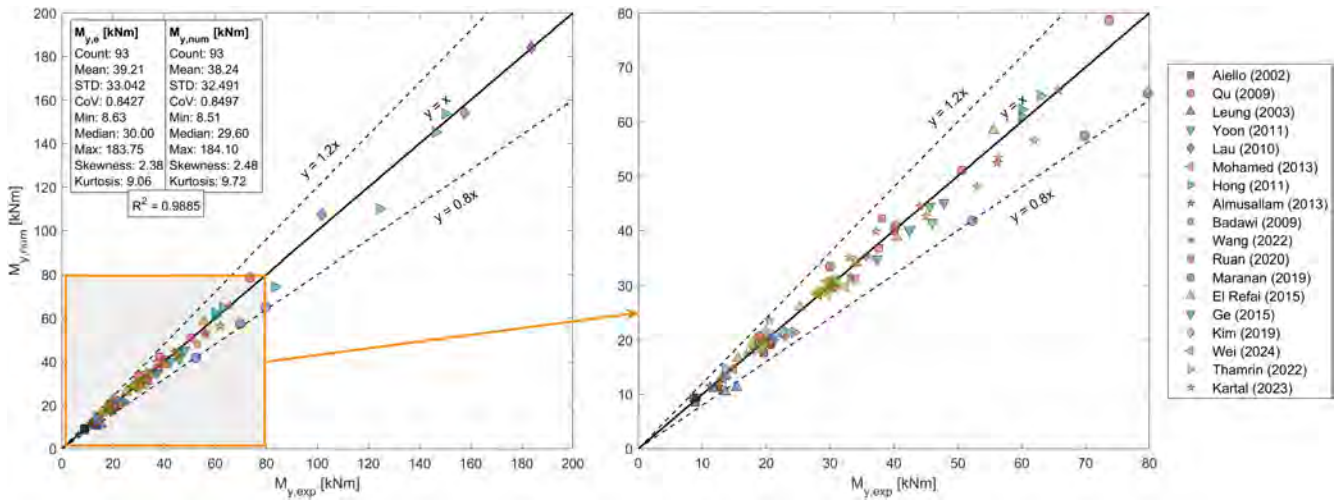


Figure 7. Relationship between experimental and theoretical yielding moments of the benchmark HRC beams.

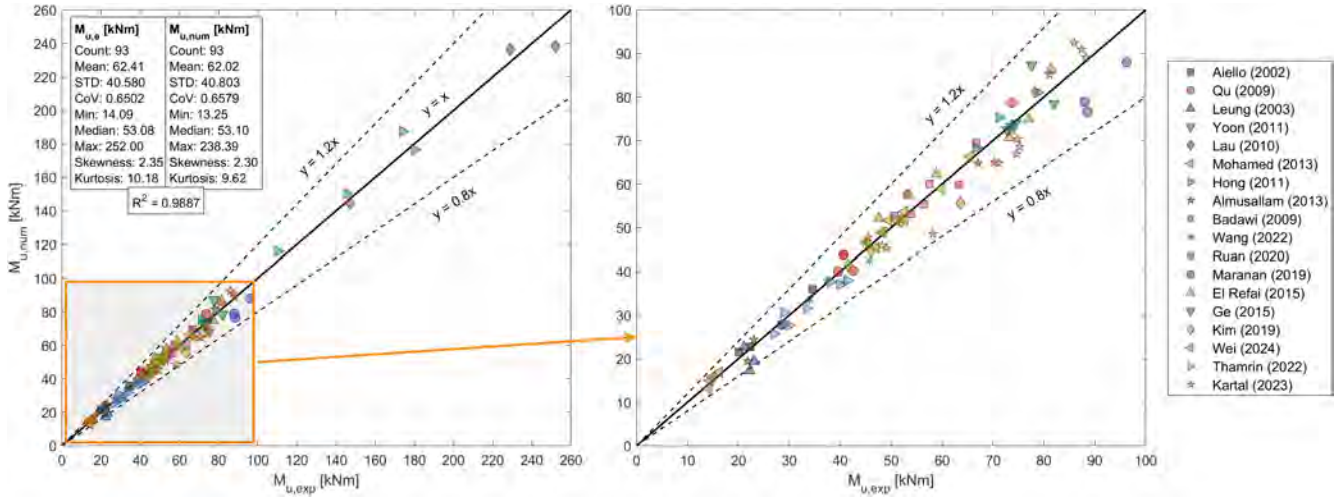


Figure 8. Relationship between experimental and theoretical ultimate moments of the benchmark HRC beams.

4.2.1. Yielding Moment

Across the 93 specimens, the mean numerical-to-experimental yielding moment ratio is 0.975. The coefficient of determination is R^2 = 0.9885. The slight underestimation captured by the mean ratio reflects the adoption of an elastic–perfectly plastic constitutive law for steel, which neglects strain hardening at the yield transition. The scatter plot in Figure 7 confirms that the predicted values cluster tightly around the line of perfect agreement. The vast majority of points lie within the ±20% deviation bands across the full range of yielding moments, from approximately 8 to 184 kNm. No systematic deviation at high or low moment levels is detected.

Among available studies in the literature, explicit validation of the yielding moment across a comprehensive database is rarely reported. Most existing models for HRC sections focus exclusively on ultimate capacity. The present validation provides a quantitative benchmark for this response quantity across all four FRP types and a wide range of reinforcement configurations.

4.2.2. Ultimate Moment

The mean numerical-to-experimental ultimate moment ratio is 0.993, with a standard deviation of 0.063 and a coefficient of variation of 6.3%. The coefficient of determination is R^2 = 0.9887. The scatter plot in Figure 8 confirms close agreement across the full range of ultimate moments, from approximately 14 to 252 kNm. All data points fall within the ±20% deviation bands. The distribution is symmetric around the line of perfect agreement, with no visible bias.

Closed-form formulations developed within the ACI 440.1R and CSA S806 frameworks have been reported in previous studies to yield mean ratios around 0.89 to 0.94 with coefficients of variation of 13 to 15%. The proposed model achieves a mean ratio closer to unity and approximately half the coefficient of variation. This improvement reflects the more refined treatment of strain compatibility, force equilibrium, and concrete compressive behavior implemented in the layer-by-layer numerical integration procedure.

4.2.3. Failure Mode Classification

The predicted failure modes align with the experimental observations. The model classifies each specimen according to the strain field at the ultimate condition. The dominant prediction is steel yielding followed by concrete crushing (SY-CC), consistent with the observed prevalence of this mechanism in the database. Cases involving steel yielding

followed by concrete crushing and FRP rupture (SY-CC-FR) are also correctly identified. This consistency between predicted and observed failure modes provides an additional indicator of the mechanical soundness of the proposed formulation.

5. Numerical Study

5.1. Dimensionless Sectional Parameters

This section presents a parametric investigation aimed at characterizing the structural response of HRC sections. Interaction domains are expressed in dimensionless form to allow consistent comparison between sections with different geometrical and mechanical properties [24]. Two sets of dimensionless parameters are used, according to the adopted design formats. Their expressions are reported in Table 5.

Table 5. Dimensionless parameters according to EN 1992-1-1 and ACI 318.

Dimensionless Parameter	EC2+CNR	ACI
Axial load, ν	$\frac{N_{Rd}}{f_{cd} \cdot b \cdot h}$	$\frac{\phi \cdot N_n}{f'_c \cdot b \cdot h}$
Bending moment, μ	$\frac{M_{Rd}}{f_{cd} \cdot b \cdot h^2}$	$\frac{\phi \cdot M_n}{f'_c \cdot b \cdot h^2}$
FRP mechanical reinf. ratio, ω_f	$\frac{A_f \cdot f_{fd}}{b \cdot h \cdot f_{cd}}$	$\frac{A_f \cdot f_{fu}}{b \cdot h \cdot f'_c}$
Steel mechanical reinf. ratio, ω_s	$\frac{A_s \cdot f_{yd}}{b \cdot h \cdot f_{cd}}$	$\frac{A_s \cdot f_y}{b \cdot h \cdot f'_c}$
Hybridization index, R	$\frac{\omega_s}{\omega_f} = \frac{A_{s,tot} \cdot f_{yd}}{A_{f,tot} \cdot f_{fd}}$	$\frac{\omega_s}{\omega_f} = \frac{A_{s,tot} \cdot f_y}{A_{f,tot} \cdot f_{fu}}$

The hybridization parameter R quantifies the relative contribution of steel and FRP longitudinal reinforcement to the tensile resistance of the section. It governs the balance between ductile and brittle reinforcement and therefore directly influences the governing failure mode and curvature capacity of hybrid sections.

Once the reinforcement design properties are fixed, variations of R can be achieved only by modifying reinforcement areas. Under this assumption, the total mechanical reinforcement ratio of an HRC section can be expressed as:

$$\omega_h = \omega_s \cdot \left(1 + \frac{1}{R}\right) = \omega_f \cdot (1 + R) \tag{23}$$

The hybrid mechanical ratio ω_h represents the total longitudinal resistant capacity normalized with respect to the concrete compressive resistance and therefore governs the global strength level of the section and the extension of both the axial force–bending moment interaction domain and the moment–curvature response.

Within this dimensionless framework, parametric investigation is performed by varying the total hybrid mechanical reinforcement ratio ω_h, the hybridization ratio R and the normalized axial load level ν, while maintaining concrete and reinforcement material properties constant. The combined variation of these parameters allows systematic identification of transition regions between FRP rupture, steel yielding followed by concrete crushing, and hybrid failure mechanisms under combined axial load and bending moment.

From a practical design perspective, ν indicates the axial load level and determines the governing failure-mode region within the N–M domain. The parameter μ quantifies the bending utilization of the section. The ratio ω_h controls the global reinforcement level and the extension of the interaction domain. The parameter R governs the balance

between steel and FRP contributions and therefore controls the failure mode, curvature ductility, and energy dissipation capacity. A professional engineer can use these four parameters to identify the reinforcement configuration that satisfies both strength and ductility requirements for a given axial load level.

5.2. Material Properties

The procedures used to derive design material strengths and the corresponding reduction coefficients are described in Section 2. The material properties adopted in the study are summarized in the following sections. Specifically, Table 6 reports the mechanical properties of concrete, Table 7 presents the properties of steel reinforcement, and Table 8 summarizes the mechanical properties of GFRP bars. The selected values are consistent with the respective European (EN 1992-1-1 and CNR-DT 203) and American (ACI 318 and ACI 440.11-22) design frameworks and are representative of conventional structural materials adopted in hybrid steel–GFRP reinforced concrete applications.

Table 6. Concrete properties according to EN 1992-1-1 and ACI 318-25.

Concrete C25/30–EN 1992-1-1			
Characteristic compressive strength	f_{ck}	25.0	MPa
Design compressive strength	f_{cd}	14.2	MPa
Compressive strain at elastic limit	ε_{c2}	2.0	‰
Ultimate compressive strain	ε_{cu}	3.5	‰
Concrete–ACI 318-25			
Specified compressive strength	f'_c	25.0	MPa
Ultimate compressive strain	ε_{cu}	3.0	‰

Table 7. Steel bar properties according to EN 1992-1-1 and ACI 318-25.

Steel B450C–EN 1992-1-1			
Tensile modulus of elasticity	E_s	200	GPa
Characteristic yield strength	f_{yk}	450.0	MPa
Characteristic yield strain	ε_{yk}	2.25	‰
Design yield strength	f_{yd}	391.3	MPa
Design yield strain	ε_{yd}	1.96	‰
Steel–ACI 318-25			
Tensile modulus of elasticity	E_s	200	GPa
Yield strength	f_y	420.0	MPa
Yield strain	ε_y	2.00	‰

Table 8. GFRP bar properties according to CNR-DT 203 and ACI 440.11-22.

ASTM D8505/D8505M-23			
Mean tensile modulus of elasticity	E_f	60	GPa
Guaranteed tensile strength	f_{fk}	898	MPa
Guaranteed tensile strain	ε_{fk}	14.967	‰
CNR-DT 203 R1/2026			
Design tensile strength	f_{fd}	431	MPa
Design tensile strain	ε_{fd}	7.184	‰
ACI 440.11-22			
Design tensile strength	f_{fu}	763.3	MPa
Design tensile strain	ε_{fu}	12.721	‰

5.3. Parametric Analysis

The parametric study is conducted on a reference HRC section with fixed geometry and material properties, as described in Section 2, which serve as the normalization basis for all dimensionless reinforcement and mechanical parameters introduced in Table 5. The section features a four-layer longitudinal reinforcement layout, with FRP bars positioned near the extreme fibers and steel reinforcement in the internal layers; this configuration defines the effective depth parameters d_s and d_f, which enter the moment calculation but do not affect the dimensionless reinforcement parameters ω_h, ω_s, ω_f, and R.

The reinforcement areas A_s and A_f are determined under EC2+CNR provisions by prescribing the hybridization coefficient R equal to 0.5, 1.0 and 2.0 and the total hybrid mechanical reinforcement ratio ω_h in the range 0.1 to 1.0 with increments of 0.1, using the material properties given in Tables 6–8. The same physical section, with identical reinforcement areas, is subsequently characterized under ACI provisions, yielding the corresponding ACI-normalized quantities ν, μ, ω_h, and R. It is worth noting that this approach replicates a realistic design scenario in which a single physical section, defined by identical geometry and reinforcement areas, is assessed under two different normative frameworks. The difference between the two normalizations arises exclusively from the distinct material strength definitions adopted by each standard, thereby enabling a direct comparison of the safety formats without altering the underlying structural configuration.

Three values of R are considered: 0.5, corresponding to a predominant FRP tensile contribution; 1.0, corresponding to comparable steel and FRP contributions; and 2.0, corresponding to a predominant steel contribution. The parametric combinations are completed by two configurations of normalized cover distances c_s/H and c_f/H, where c_s and c_f denote the distance between the centroid of the steel and FRP reinforcement layers and the nearest edge of the cross-section, respectively, as summarized in Table 9.

Table 9. Investigated parametric combinations of section geometry and reinforcement.

ID	$R_{EC2+CNR}$	R_{ACI}	c_f/H	c_s/H
S-20-A S-20-B	2.00	1.213	0.1 0.05	0.2 0.1
S-10-A S-10-B	1.00	0.606	0.1 0.05	0.2 0.1
S-05-A S-05-B	0.50	0.303	0.1 0.05	0.2 0.1

Figure 9 illustrates the decomposition of ω_h into its steel and FRP components, ω_s and ω_f, for the three values of R. For a fixed ω_h, increasing R redistributes the total tensile mechanical capacity toward the steel contribution, resulting in higher ω_s and lower ω_f while preserving the global normalized capacity. The hybridization coefficient R therefore governs not only the relative reinforcement areas but also the expected strain regime and the controlling failure mode under combined axial force and bending.

The A_f-A_s diagrams in Figures 10 and 11 report the balanced failure mode boundaries BFM 2-3 and BFM 3-4a for each parametric configuration, computed according to the EC2+CNR framework. The markers identify the investigated parametric configurations, each corresponding to a discrete combination of steel and FRP reinforcement areas (A_s, A_f) associated with prescribed values of ω_h and R. The green lines (BFM 2-3) separate the FRP rupture-controlled domain (FM-2) from the steel-yielding-controlled domain (FM-3); the red lines (BFM 3-4a) bound the transition toward concrete crushing-controlled failure (FM-4a). Increasing ω_h from 0.1 to 1.0 shifts the design configurations progressively from FM-2 toward FM-3, reflecting the growing steel contribution to tensile capacity and the

associated enhancement in deformation capacity prior to concrete crushing. It is worth noting that the BFM boundary lines are not universal: their position depends explicitly on the applied axial load level N_{Ed}, which enters directly into the intercept expressions of Equations (9) and (14). As a consequence, a parametric configuration may fall in different failure mode domains depending on the applied axial load level. Each marker is therefore associated with a corresponding pair of BFM boundary lines, one green (BFM 2-3) and one red (BFM 3-4a), whose relative position with respect to the marker determines the governing failure mode of that configuration.

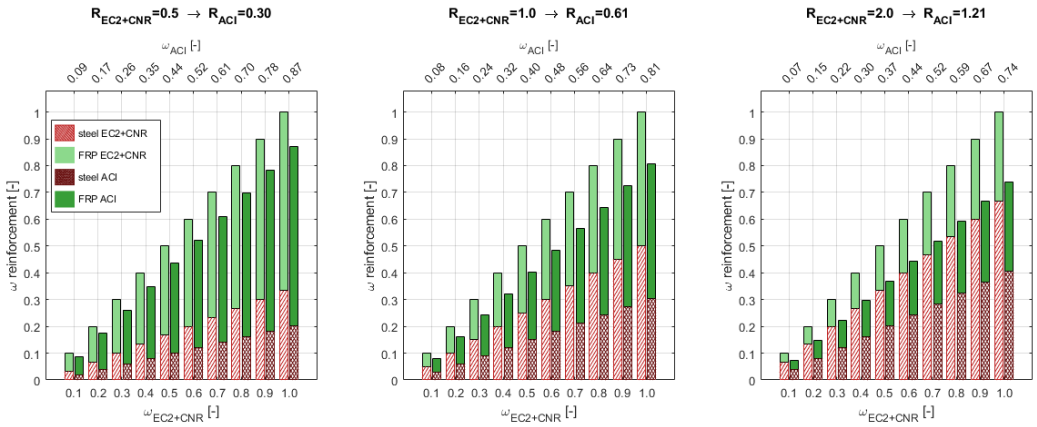


Figure 9. Hybrid reinforcement ratio components distribution for different R values.

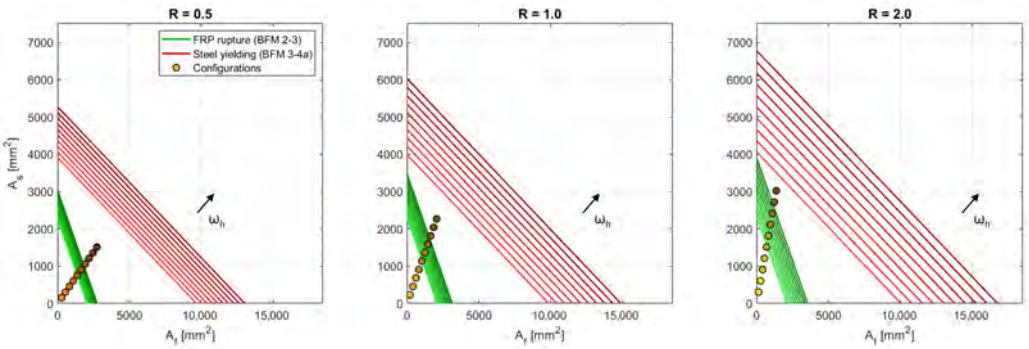


Figure 10. A_f-A_s diagram failure mode domain of the sectional groups A under pure bending regime, according to the EC2+CNR framework.

Figure 10 presents the BFM boundaries under pure bending ($\nu = 0$). Increasing ω_h displaces the configurations progressively toward larger reinforcement areas, with a concurrent outward translation of the BFM boundaries. The trajectory of the configurations in the A_f-A_s plane is controlled by R: higher R values produce a displacement predominantly along the A_s axis, reflecting a proportionally greater steel contribution, whereas lower R values yield a displacement predominantly along the A_f axis, consistent with a larger relative FRP contribution.

Figure 11 illustrates the influence of compressive axial force on the balanced failure boundaries, evaluated at a normalized axial load level $\nu = 0.1$. Increasing axial compression translates the BFM boundaries toward the origin, reducing both intercepts and causing configurations classified within the FM-3 domain under pure bending to shift toward FM-2 or FM-4a. Under elevated compression, sections with moderate ω_f may exhibit concrete crushing prior to FRP rupture, producing a sectional response analogous to that of more heavily reinforced configurations under pure bending.

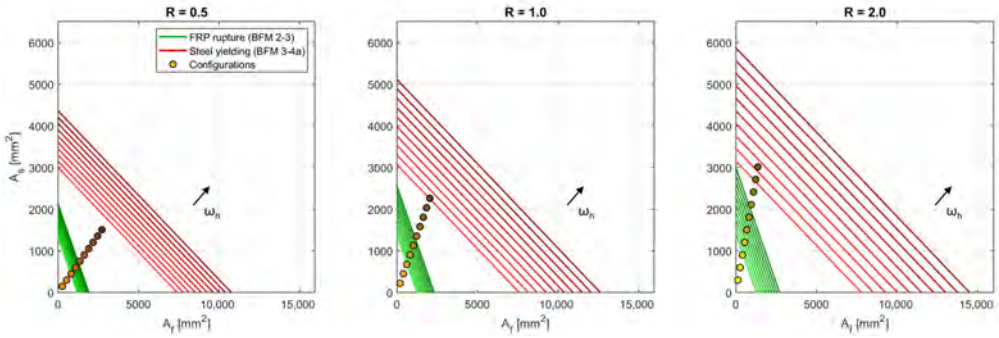


Figure 11. A_f-A_s diagram failure mode domain of the sectional Group A under combined axial load and bending regime at $\nu = 0.1$, according to the EC2+CNR framework.

5.4. ν-μ Interaction Domains

5.4.1. European Framework

The parametric results for the European framework (EC2+CNR) are presented in Figure 12 (Group A, i.e., with $c_f/H = 0.1$ and $c_s/H = 0.2$) and Figure 13 (Group B, i.e., with $c_f/H = 0.05$ and $c_s/H = 0.1$), showing the ν-μ interaction domains for a total of 60 sections, 30 per group, covering three hybridization ratios ($R = 0.5$, 1.0, 2.0) and ten hybrid mechanical reinforcement ratios ($\omega_h = 0.1$ to 1.0). The results demonstrate that increasing ω_h produces a global expansion of the ν-μ interaction domain, with a more pronounced increase at the BFM 2-3 transition boundary, indicating a stronger sensitivity of steel-yielding transitions to the total reinforcement level relative to compression-controlled transitions. Increasing R shifts both the BFM 3-4a and BFM 2-3 transitions toward higher axial compression and moment levels. A systematic influence of the reinforcement layout is observed: Group B sections (Figure 13) exhibit higher BFM 2-3 and BFM 3-4a transition values than Group A sections (Figure 12), consistent with the smaller cover distances adopted in Group B, which increase the effective lever arm of both steel and FRP reinforcement, thereby enhancing the sectional flexural capacity under combined axial force and bending moment.

5.4.2. American Framework

Figure 14 (Group A) and Figure 15 (Group B) show the ν-μ interaction domains for the same 60 sections designed according to the American framework (ACI 318-25 and ACI 440.11-22). In each figure, dashed curves represent nominal capacities, while solid curves represent design capacities reduced by the strain-dependent SRF. The nominal interaction domains are comparable in extent to those obtained within the European framework. The reduction introduced by the SRF is most significant in the compression-controlled region ($\nu < 0$), where the gap between nominal and design domains is largest, while in the tension-controlled region ($\nu > 0$) the two sets of curves remain closely aligned. The value of $\phi = 0.90$ is applied consistently across all tension-controlled configurations, as indicated in the subplot titles of the μ-χ diagrams. A further distinctive feature of the ACI design domain is the vertical cutoff on the left part that corresponds to the maximum design axial load limit imposed by ACI 318-25. This limit, which has no counterpart in the European framework, truncates the design domain at an axial compression level that depends on the steel reinforcement content and gross sectional area, as the FRP contribution is neglected under pure compression conditions according to ACI provisions.

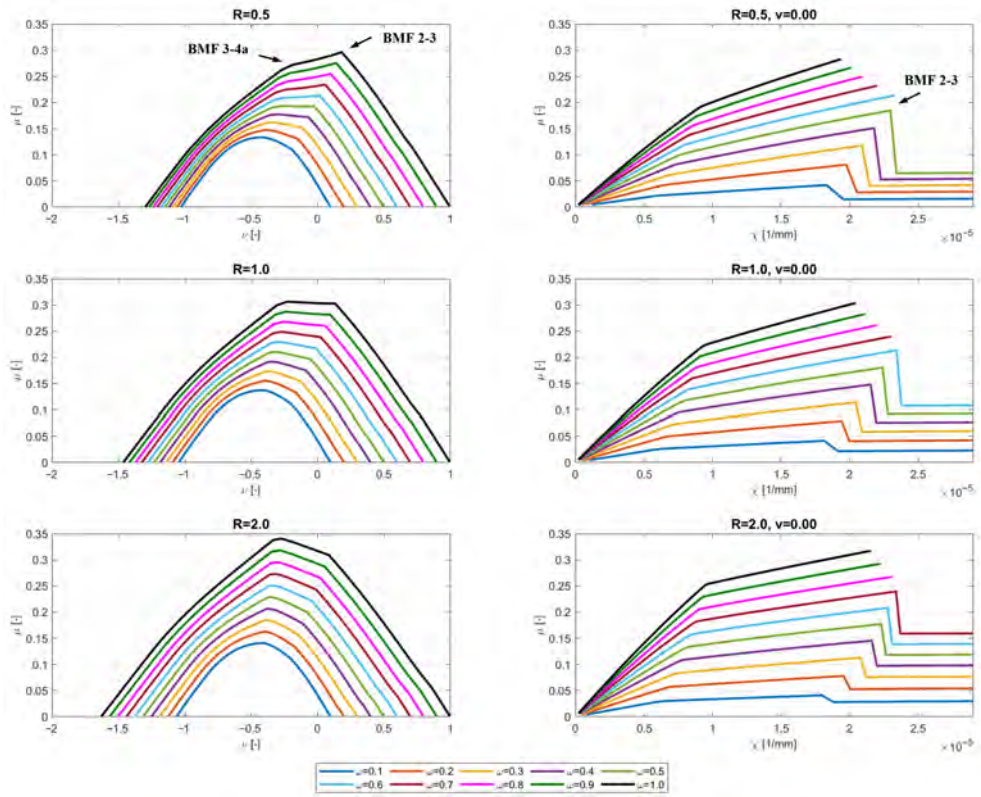


Figure 12. Section Group A dimensionless diagrams according to EC2 and CNR.

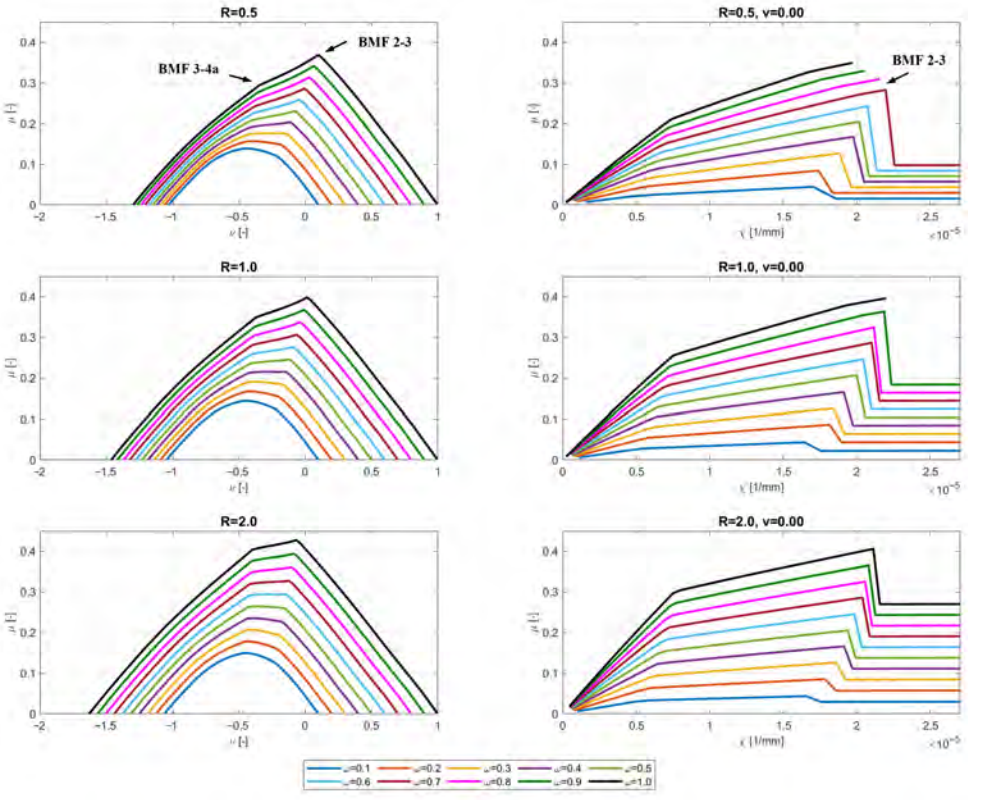


Figure 13. Section Group B dimensionless diagrams according to EC2 and CNR.

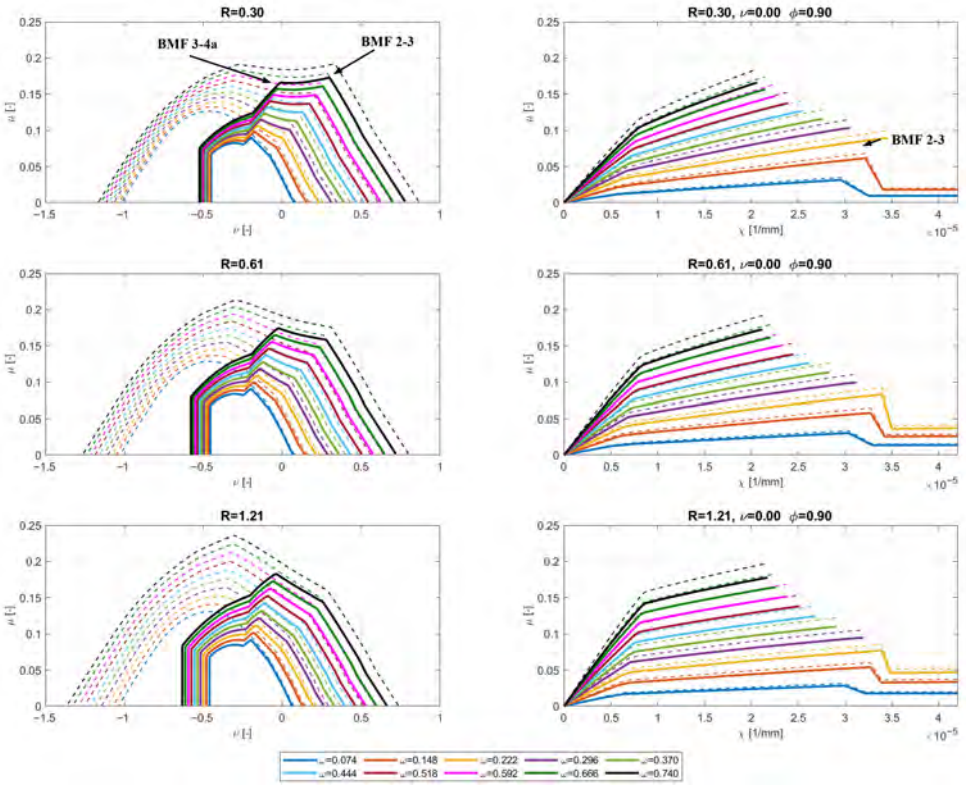


Figure 14. Section Group A nominal (dashed) and design (solid) dimensionless diagrams according to ACI.

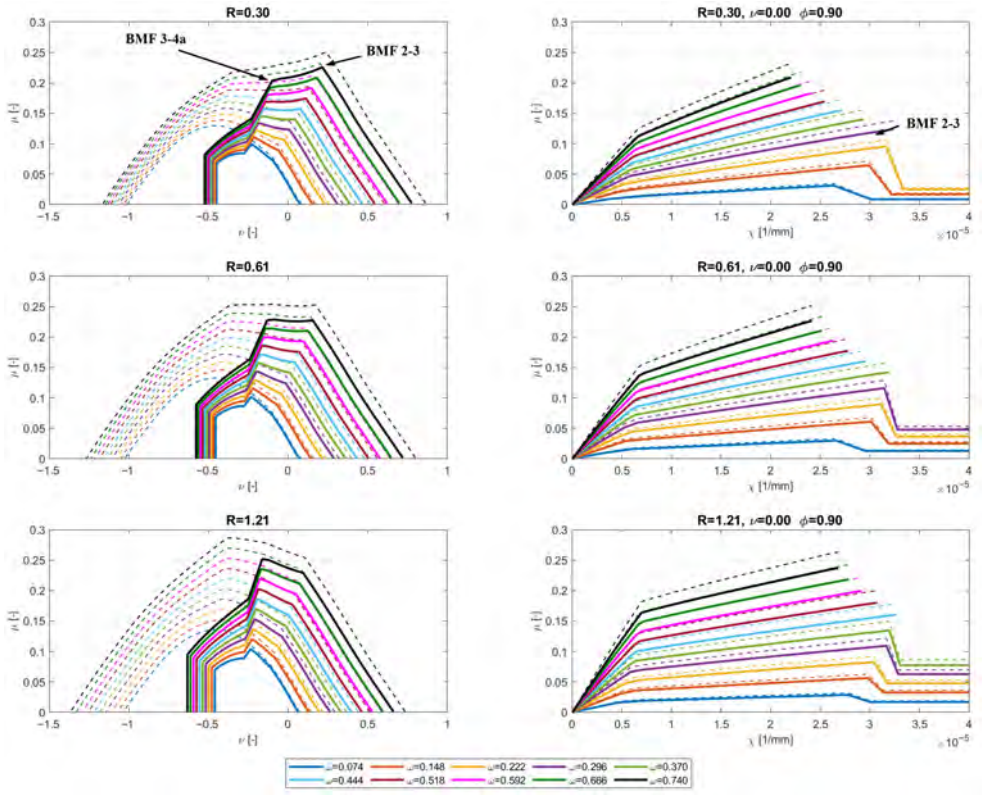


Figure 15. Section Group B nominal (dashed) and design (solid) dimensionless diagrams according to ACI.

5.5. M–χ Response Under Zero Axial Load ν

5.5.1. European Framework

The μ-χ responses at $\nu = 0$ are shown in the right column of Figure 12 for Group A and in the right column of Figure 13 for Group B. For Group A, the FM-2 to FM-3 transition occurs at approximately $\omega_h = 0.5$ for $R = 0.5$, $\omega_h = 0.6$ for $R = 1.0$, and $\omega_h = 0.7$ for $R = 2.0$. Beyond this threshold, χ_{peak} decreases while μ_{peak}, μ_y and χ_y continue to increase, confirming that the FM-2 to FM-3 transition reduces ultimate deformation capacity without affecting flexural strength or the yielding response. The shift of the transition threshold toward higher ω_h as R increases indicates that a larger steel contribution extends the ω_h range over which FM-2 governs, delaying the transition to FM-3.

For Group B, the transition occurs at values of ω_h higher than those relative to Group A. For $R = 0.5$, the FM-2 to FM-3 transition begins at approximately $\omega_h = 0.7$. For $R = 1.0$, only the configuration with $\omega_h = 1.0$ reaches FM-3, while lower ω_h levels remain governed by FM-2. For $R = 2.0$, all investigated configurations remain governed by FM-2, indicating that the increased lever arm of Group B maintains FRP rupture as the governing failure mechanism over a wider reinforcement range.

Increasing R at constant axial load produces a progressive increase in both μ_{peak} and μ_y, while χ_y remains approximately unchanged and χ_{peak} increases moderately within the FM-2 regime, confirming that hybridization primarily enhances flexural strength rather than modifying the deformation threshold associated with steel activation.

5.5.2. American Framework

The μ-χ responses at $\nu = 0$ for the American framework are shown in the right column of Figure 14 for Group A and in the right column of Figure 15 for Group B. The same failure mode characteristics observed in the European framework are confirmed: sections governed by FM-2 exhibit an abrupt drop in moment capacity due to FRP rupture followed by a horizontal plateau, while sections governed by FM-3 terminate more gradually. The application of the SRF reduces the design moment response relative to the nominal curves, affecting both yielding moment (μ_y) and peak moment (μ_{peak}), while curvature quantities (χ_y, χ_{peak}) remain at their nominal values. The reduction is more pronounced for sections in the tension-controlled regime.

5.6. Influence of Axial Load Level ν

The combined influence of R, ω_h and ν is illustrated in Figure 16 for the European framework and in Figure 17 for the American framework, for $\nu = 0.10$, 0.25 and 0.50, corresponding to increasing levels of compressive axial load. Axial compression modifies both the governing failure mechanism and the moment–curvature response: increasing ν reduces peak moment and curvature at higher ω_h, while at $\nu = 0.50$ ultimate curvature stabilizes and becomes insensitive to ω_h. Increasing R raises peak moment at constant axial load, with comparatively moderate effects on curvature capacity.

For $\omega_h \lesssim 0.3$, moderate axial compression increases μ_{peak} in both frameworks: compression shifts the neutral axis in a way that enhances the internal lever arm of the tensile reinforcement without triggering premature concrete crushing. For $\omega_h \gtrsim 0.4$, μ_{peak} continues to grow with ω_h regardless of ν, as the steel contribution to flexural strength in the FM-3 regime more than offsets the compression-induced reduction in the tensile zone. Within the American framework, the strain-dependent factor $\phi(\varepsilon_s)$ introduces an additional reduction that becomes increasingly penalising as conditions shift toward compression-controlled behavior, widening the gap between EC2+CNR and ACI predictions with increasing ν. As shown in Figure 17, the range of ϕ values narrows progressively with increasing com-

pression: from $\phi = 0.81 \div 0.90$ at $\nu = 0.10$ to $\phi = 0.65$ at $\nu = 0.50$, reflecting the transition toward fully compression-controlled behavior where ϕ is no longer strain-dependent.

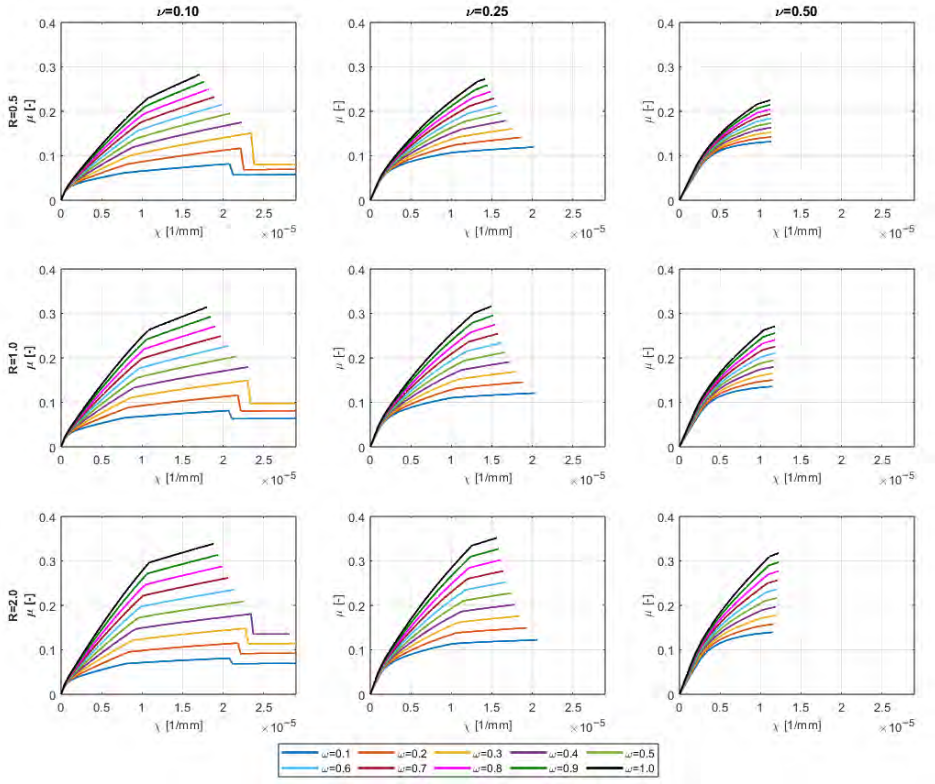


Figure 16. Combined effect of ω_h, ν and R ratios on M–χ relationships according to EC2 and CNR.

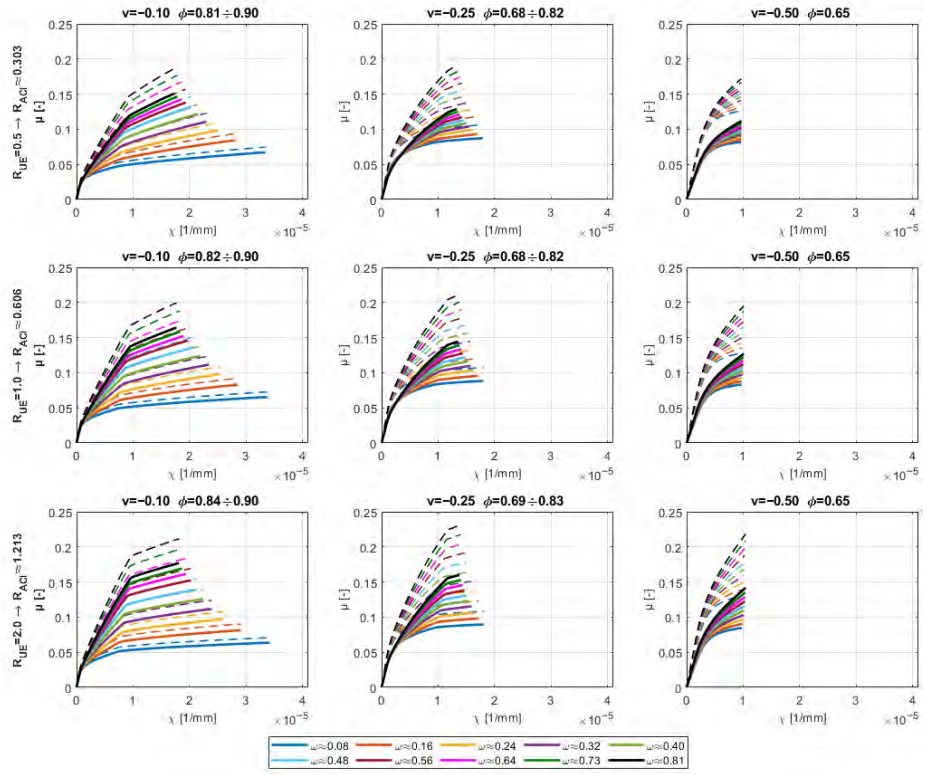


Figure 17. Combined effect of ω_h, ν and R ratios on M–χ relationships according to ACI.

Curvature capacity exhibits a non-monotonic dependence on ω_h and ν in both frameworks, reflecting transitions between failure mechanisms. For $\omega_h \lesssim 0.3$, χ_{peak} increases with moderate compression, consistent with the FM-2 regime in which compression delays FRP rupture by reducing tensile strain demand. For $\omega_h \gtrsim 0.4$, the rate of increase in χ_{peak} with ω_h diminishes progressively at higher ν, owing to earlier attainment of the concrete compressive strain limit. At $\nu = 0.50$, χ_u stabilizes and becomes insensitive to ω_h, converging to a value governed by ε_{cu}/x_u: compression-controlled conditions constrain the strain field near the crushing limit regardless of reinforcement content, so that section geometry rather than reinforcement configuration determines ultimate curvature. This saturation is observed in both frameworks; within the ACI framework, the decrease in ϕ under compression-controlled conditions further reduces design moment capacity relative to European predictions, producing a penalty on flexural resistance absent in the EC2+CNR safety format.

At $\nu = 0.10$ and low ω_h, a pronounced nonlinearity is visible in the pre-yield branch of the moment–curvature response, progressively disappearing as ω_h increases. At low ω_h, FRP reinforcement, whose elastic-linear response extends to rupture without yielding, dominates tensile stiffness; the gradual neutral axis shift under increasing curvature produces a non-proportional stress redistribution between FRP and concrete, manifesting as pre-yield nonlinearity. At high ω_h, steel dominates sectional stiffness and its bilinear constitutive response regularises the pre-yield branch, masking the FRP contribution. Within the ACI framework, this feature is partially attenuated by the uniform scaling of ϕ, which reduces the amplitude of the nonlinear branch without altering its physical origin.

At $\nu = 0.50$, compression suppresses steel yielding entirely across the majority of configurations: the concrete compressive strain limit is reached before ε_{yd} is attained, μ_y and χ_y are undefined, and the ductility factor is not applicable. A distinctive feature of the American framework is the identification of configurations governed solely by steel yielding without FRP rupture, not encountered in the European framework for the same physical sections. This reflects the more conservative FRP design strengths of ACI 440.11-22 relative to CNR-DT 203 R1/2026, which reduce tensile FRP demand and shift the governing failure mechanism toward steel yielding across a wider reinforcement range.

The observed failure mode transitions are governed by neutral axis migration under increasing axial compression. When ν increases, the neutral axis shifts toward the tension side of the section. This reduces the tensile strain available at the reinforcement level for a given compressive strain at the top fiber. The concrete extreme fiber reaches ε_{cu} before the FRP bars attain their ultimate strain ε_{fu}. The section therefore transitions from FM-2, where FRP rupture governs, to FM-3 or FM-4a, where concrete crushing controls. This transition occurs at progressively lower values of ω_h as ν increases, because the additional compression further constrains the tensile strain field. The saturation of ultimate curvature χ_u at $\nu = 0.50$ results from the same mechanism. At high axial load levels, the curvature is constrained by the ratio ε_{cu}/x, where x is the neutral axis depth. Since both ε_{cu} and x become nearly insensitive to ω_h in the compression-controlled regime, χ_u stabilizes regardless of reinforcement content.

5.7. Ductility Estimation

Ductility estimation is introduced to provide a deformation-capacity indicator for HRC sections governed by steel-yield-controlled failure modes, particularly within FM-2 and FM-3 domains. The curvature ductility factor is adopted as representative indicator of deformation capacity, and it is defined as:

$$D_{des} = \frac{\chi_u}{\chi_y} \tag{24}$$

where χ_u is the ultimate curvature and χ_y is the curvature at first steel yielding. This definition is adopted for both the European (EC2+CNR) and American (ACI) design frameworks.

Ductility was assessed for Group A and Group B sections under normalized axial load levels up to $\nu = 0.25$. Results are reported in Figure 18 (EC2+CNR) and Figure 19 (ACI). Across all configurations, increasing axial compression reduces sectional ductility, driven by earlier attainment of the concrete compressive strain limit and a progressive shift toward compression-controlled failure.

For Group A sections within the European framework (Figure 18, left), ductility under zero axial load remains approximately constant up to $\omega_h \approx 0.6$ and then decreases. At $\nu = 0.10$, the plateau shortens to $\omega_h \approx 0.3$. At $\nu = 0.25$, ductility decreases monotonically across the full ω_h range. For Group B sections (Figure 18, right), a broader plateau is observed at low axial load: ductility remains nearly constant across the full ω_h range at $\nu = 0$, and up to $\omega_h \approx 0.5$ at $\nu = 0.10$. At higher axial load the decreasing trend becomes dominant. Group B sections consistently exhibit higher ductility than Group A sections at equivalent ω_h and ν levels, owing to the increased effective lever arm associated with the smaller cover distances of Group B.

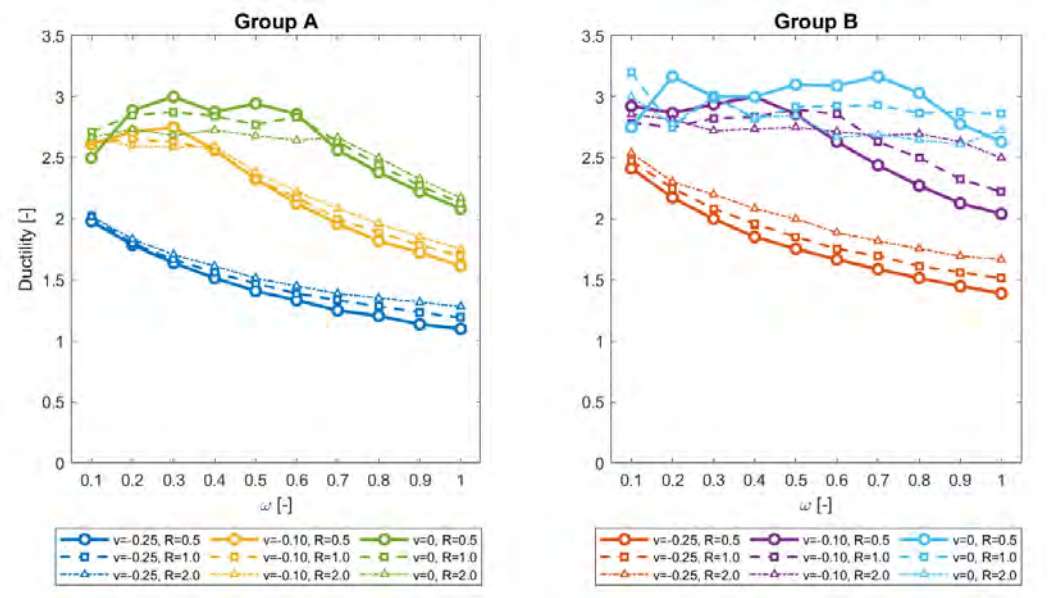


Figure 18. Ductility according to EC2 and CNR.

Consistent trends are observed within the American framework (Figure 19). For Group A sections, ductility at zero axial load reaches a peak at $\omega_h \approx 0.2$–0.3 for $R = 0.303$, and then decreases monotonically. At $\nu = 0.10$ and 0.25, the peak shifts toward lower ω_h values and the overall ductility level is reduced. For Group B sections, higher ductility values are observed at low ω_h for $\nu = 0$, particularly for lower R values. Across all configurations, ductility decreases across the entire ω_h range at higher axial compression, confirming the dominant influence of axial compression on deformation capacity independently of the design framework.

The influence of hybridization ratio R on ductility is not monotonic and depends on the ω_h range and reinforcement layout. Within the European framework, lower R values tend to correspond to higher ductility at low-to-moderate ω_h, but this ordering is not preserved at higher reinforcement levels, where the curves converge or cross. Within the ACI framework, for Group A sections, higher ductility is associated with configurations characterized by a larger relative FRP contribution, provided the governing failure mode remains steel yielding without FRP rupture activation: under these conditions, the section exploits the full deformation capacity associated with steel yielding while retaining the

stiffness contribution of FRP. This trend is not observed for Group B sections, where the relationship between R and ductility depends more strongly on the specific failure mechanism activated within each configuration.

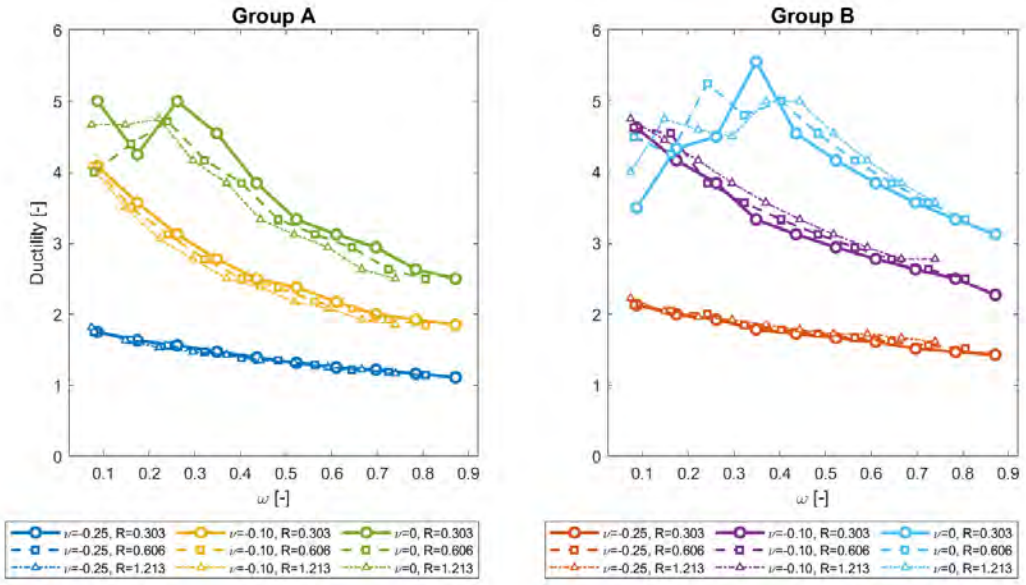


Figure 19. Ductility according to ACI.

5.8. Energy Dissipation

Energy dissipation provides a complementary indicator of ultimate limit state behavior, quantifying the area under the moment–curvature response beyond what sectional ductility alone captures. The same configurations considered in the ductility assessment were evaluated; results are reported in Figure 20 (EC2+CNR) and Figure 21 (ACI).

Group A sections systematically exhibit lower energy dissipation than Group B across both frameworks. This difference reflects the reinforcement layout: in Group B, steel and FRP are positioned closer to the external fibers, increasing the internal lever arm, promoting larger curvature development prior to failure, and consequently enlarging the area under the response.

Within Group A, the ACI framework predicts lower design energy dissipation than EC2+CNR, particularly for $\omega_h \gtrsim 0.7$, where the strain-dependent reduction in ϕ reduces the design moment ordinates of the moment–curvature response. Across all configurations, dissipated energy increases rapidly with ω_h while the response is governed by FM-2 FRP rupture. As ω_h enters the FM-3 steel-yielding regime, the rate of increase reduces, producing a bilinear trend that reflects the transition from FRP-controlled failure toward steel yielding. This bilinear behavior progressively attenuates with increasing axial load and disappears at $\nu = -0.25$, where compression-controlled conditions limit curvature development and suppress the energy accumulation associated with steel yielding. In the ACI framework, Group B sections reach significantly higher dissipated energy values than Group A at equivalent ω_h and ν levels, confirming the dominant role of the reinforcement layout on energy dissipation capacity.

The non-monotonic relationship between R and curvature ductility is explained by competing effects of the two reinforcement types. At low R values, the dominant FRP contribution provides high tensile stiffness but limits ductility because of the brittle FRP failure mode. Increasing R, the proportion of steel reinforcement raises. Steel bars, having a lower elastic modulus than FRP bars, attract a smaller share of the tensile force at equal strain. This reduces the strain demand on the FRP bars and delays the attainment of ε_{fu}. The larger steel component yields before ULS, enhancing energy dissipation and curvature

ductility. Beyond a critical R value, the reduced FRP content lowers the overall tensile capacity of the section. This leads to a shallower post-yielding branch and earlier concrete crushing. The net effect is a peak in curvature ductility at an intermediate R value that depends on ω_h and ν.

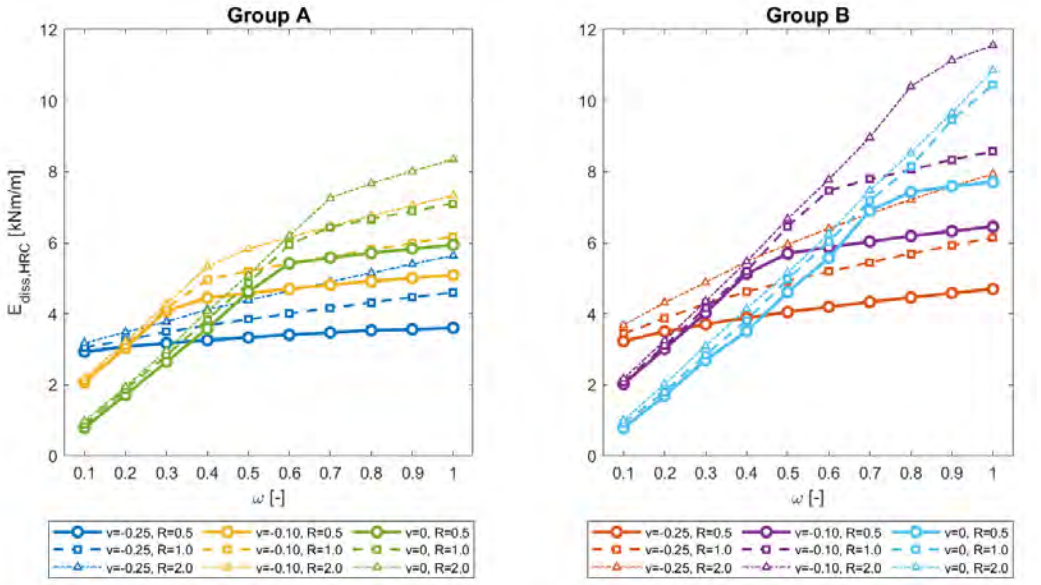


Figure 20. Dissipated energy according to EC2 and CNR.

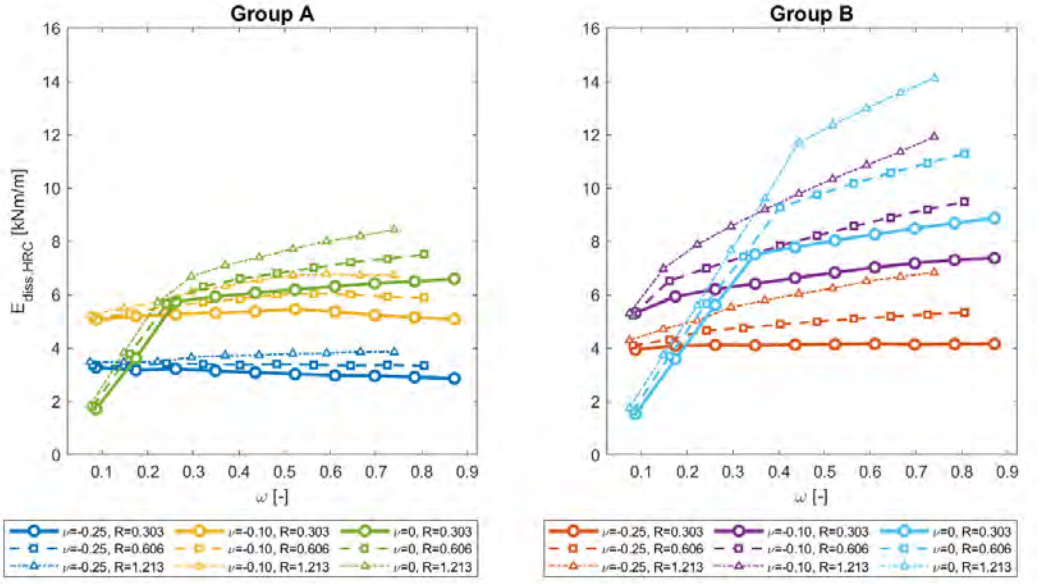


Figure 21. Dissipated energy according to ACI.

6. Conclusions

The present study developed a parametric approach for the ULS assessment of HRC sections, incorporating an inner layer of steel reinforcement and an outer layer of FRP bars under combined axial force and bending moment. A sectional model based on strain compatibility and force equilibrium was implemented through a LLNI procedure to generate N–M interaction domains and M–χ relationships within both European (EC2+CNR) and American (ACI 318-25 and ACI 440.11-22) normative frameworks. The dimensionless formulation in terms of ν, μ, ω_h and R enabled systematic comparison between hybrid configurations and identification of balanced failure transitions.

The main findings may be summarized as follows:

- The proposed validation against a benchmark database of 93 hybrid reinforced concrete beams collected from 18 independent experimental campaigns demonstrated the reliability of the sectional model in modeling HRC members. The mean numerical-to-experimental ratio is 0.975 for the yielding moment (CoV = 7.7%, R^2 = 0.9885) and 0.993 for the ultimate moment (CoV = 6.3%, R^2 = 0.9887). The predicted failure modes are consistent with the experimental observations across all four FRP types (GFRP, CFRP, BFRP, AFRP). These results confirm the reliability of the model and provide the basis for the parametric investigation developed in the subsequent sections.
- Increasing ω_h produces a global expansion of the N–M interaction domain, with a pronounced increase at the BFM 2-3 transition, reflecting the growing influence of steel yielding on sectional resistance.
- Increasing R shifts the BFM 3-4a transition toward higher axial compression and bending levels, indicating delayed FRP rupture and enhanced steel participation in the tensile response.
- As ω_h and R increase, the governing failure mechanism evolves from FRP rupture (FM-2) toward steel yielding followed by concrete crushing (FM-3), with transition thresholds dependent on reinforcement layout and cover distances.
- Under zero axial load, both frameworks predict a reduction in curvature ductility with increasing ω_h, consistent with the linear-elastic brittle response of FRP reinforcement.
- Axial compression modifies both the governing failure mechanism and the moment–curvature response. Increasing ν reduces peak moment and curvature at higher ω_h. At $\nu = 0.25$, compression-controlled conditions become dominant and suppress the bilinear energy accumulation associated with steel yielding. At $\nu = 0.50$, ultimate curvature stabilizes and becomes insensitive to ω_h, governed by section geometry rather than reinforcement configuration.
- Dissipated energy increases with ω_h in the FM-2 regime; the rate of increase reduces upon transition to FM-3.

Systematic differences are observed between the two regulatory frameworks:

- The European provisions generally predict FRP rupture (FM-2) at ultimate conditions and do not apply a strain-dependent strength reduction, resulting in higher design curvature and energy dissipation capacities relative to the American framework.
- The American provisions incorporate a strain-dependent ϕ factor that contracts the interaction domain under compression-controlled conditions and penalizes moment capacity and energy dissipation. Curvature quantities remain at their nominal values, and therefore the penalty is limited to the moment ordinate of the design response, unlike the EC2+CNR safety format where no strain-dependent reduction is applied.
- The American framework identifies configurations governed solely by steel yielding without FRP rupture activation across a wider reinforcement range, reflecting the more conservative FRP design strengths of ACI 440.11-22 relative to CNR-DT 203 R1/2026.
- The effect of R on ductility is not monotonic and depends on ω_h range and reinforcement layout; within the ACI framework, higher FRP contribution can increase ductility in Group A sections provided steel yielding remains the governing failure mode.

Author Contributions: Data curation, M.M. and G.M.; formal analysis, M.M. and G.M.; methodology, M.M.; validation, M.M.; writing—original draft preparation, M.M. and G.M.; writing—review and editing, M.M. and M.C.; conceptualization, D.M. and M.C.; supervision, M.C.; funding acquisition, D.M. All authors have read and agreed to the published version of the manuscript.

Funding: This research was financially supported by MUR—DM 352/2022, co-funded by Masera Engineering Group S.r.l. (Torino, Italy) under the PNRR–NGEU action.

Data Availability Statement: All data generated and analyzed during this study are available in the Zenodo repository at: https://doi.org/10.5281/zenodo.19487971.

Conflicts of Interest: Davide Masera is the CEO of Masera Engineering Group S.r.l., a civil engineering firm that co-funded the PhD scholarship of Mattia Mairone within the action of the Italian Ministry of University of Research DM 352/2022.

Appendix A. Benchmark Database for Model Validation

This appendix reports the complete geometric and mechanical properties of the 93 hybrid reinforced concrete beams used for the model validation presented in Section 4.

Table A1. Experimental database of FRP-reinforced concrete beams collected from the literature.

Reference	Beam	$b \times h$ [mm^2]	f'_c [MPa]	f_y [MPa]	f_{fu} [MPa]	A_s [mm^2]	A_f [mm^2]	A'_s [mm^2]	E_f [GPa]	y_s [mm]	y_f [mm]	y'_s [mm]	FRP Type
Aiello (2002) [8]	A1	150 × 200	45.7	465.0	1674.0	101.0	88.0	101.0	49.0	50	25	25	AFRP
	A2	150 × 200	45.7	465.0	1366.0	101.0	157.0	101.0	50.1	50	25	25	AFRP
	A3	150 × 200	45.7	465.0	1366.0	226.0	236.0	101.0	50.1	50	25	25	AFRP
	C1	150 × 200	45.7	465.0	1366.0	101.0	88.0	101.0	49.0	25	25	25	AFRP
Qu (2009) [9]	B3	180 × 250	33.1	336.0	782.0	226.1	253.2	157.0	45.0	30	25	30	GFRP
	B4	180 × 250	33.1	336.0	755.0	201.0	396.9	157.0	41.0	30	25	30	GFRP
	B5	180 × 250	34.4	336.0	778.0	401.9	141.7	157.0	37.7	30	25	30	GFRP
	B6	180 × 250	34.4	336.0	782.0	401.9	253.2	157.0	45.0	30	25	30	GFRP
	B7	180 × 250	40.7	336.0	778.0	113.0	141.7	157.0	37.7	30	25	30	GFRP
Lueng (2003) [49]	L2	150 × 200	28.5	460.0	760.0	157.0	141.7	157.0	40.8	70	40	40	GFRP
	L5	150 × 200	28.5	460.0	760.0	235.5	212.5	157.0	40.8	70	40	40	GFRP
	H2	150 × 200	48.5	460.0	760.0	157.0	141.7	157.0	40.8	70	40	40	GFRP
Yoon (2011) [50]	CS	230 × 250	75.9	470.0	2130.0	485.0	128.0	56.5	146.2	88	44	40	CFRP
	GS	230 × 250	75.9	470.0	941.0	485.0	381.0	56.5	48.1	88	44	40	GFRP
Lau (2010) [51]	G0.3-MD1.0-A90	280 × 380	41.3	336.0	588.0	981.7	283.5	56.5	39.5	40	35	25	GFRP
	G1.0-T0.7-A90	280 × 380	39.8	597.0	582.0	628.3	981.7	56.5	38.0	40	35	25	GFRP
	G0.6-T1.0-A90	280 × 380	44.6	550.0	588.0	981.7	567.1	56.5	39.5	40	35	25	GFRP
Mohamed (2013) [52]	B10|8S	100 × 200	30.0	530.0	755.0	157.0	100.6	100.6	39.0	65	20	65	GFRP
	B10|6S	100 × 200	30.0	530.0	780.0	157.0	56.6	100.6	41.0	65	20	65	GFRP
	B12|8S	100 × 200	30.0	470.0	755.0	226.0	100.6	100.6	39.0	65	20	65	GFRP
	B12|6S	100 × 200	30.0	470.0	780.0	226.0	56.6	100.6	41.0	65	20	65	GFRP
Hong (2011) [53]	ALII-2	250 × 400	27.0	525.0	2850.0	596.0	56.0	142.0	165.0	44	44	44	CFRP
	AMI-2	250 × 400	34.0	525.0	2850.0	380.0	56.0	142.0	165.0	44	44	44	CFRP
	AMIII-2	250 × 400	34.0	512.0	2850.0	860.0	56.0	142.0	165.0	44	44	44	CFRP
	AMIII-3	250 × 400	34.0	512.0	2850.0	860.0	84.0	142.0	165.0	44	44	44	CFRP
	BMIV-1	400 × 200	34.0	512.0	2850.0	860.0	28.0	142.0	165.0	44	44	44	CFRP
	BMIV-2	400 × 200	34.0	512.0	2850.0	860.0	56.0	142.0	165.0	44	44	44	CFRP
	BMIV-3	400 × 200	34.0	512.0	2850.0	860.0	84.0	142.0	165.0	44	44	44	CFRP
Almusallam (2013) [54]	RW1F	150 × 200	36.6	408.0	743.0	157.1	78.5	28.3	40.0	30	15	25	GFRP
	RW2F	150 × 200	36.6	408.0	743.0	78.5	157.1	28.3	40.0	30	15	25	GFRP
Badawi (2009) [55]	NonPrs	152 × 254	45.0	440.0	1970.0	400.0	70.9	200.0	136.0	45	45	45	CFRP
Wang (2022) [56]	B1.09-S0.25-0.23	150 × 250	38.2	492.0	1077.0	78.5	339.3	157.1	50.0	35	35	25	BFRP
	B0.75-S0.36-0.48	150 × 250	38.2	495.0	1166.0	113.1	235.6	157.1	51.3	35	35	25	BFRP
	B0.55-S0.53-0.96	150 × 250	38.2	478.0	1166.0	150.8	157.1	157.1	51.3	35	35	25	BFRP
	B0.52-S0.52-1.00	150 × 250	38.2	478.0	1220.0	150.8	150.8	157.1	51.5	35	35	25	BFRP
	B0.35-S0.54-1.56	150 × 250	38.2	492.0	1220.0	157.1	100.5	157.1	51.5	35	35	25	BFRP
Ruan (2020) [57]	2G12-2S12	180 × 300	30.3	517.0	868.2	226.2	226.2	100.5	40.1	35	35	30	GFRP
	2G16-2S12	180 × 300	30.3	517.0	958.2	226.2	402.1	100.5	45.7	35	35	30	GFRP
	2G12-1S16	180 × 300	30.3	540.0	868.2	201.1	226.2	100.5	40.1	35	35	30	GFRP
	2G16-1S16	180 × 300	30.3	540.0	958.2	201.1	402.1	100.5	45.7	35	35	30	GFRP
	2G12-2S12 (D)	180 × 300	30.3	517.0	868.2	226.2	226.2	100.5	40.1	60	35	30	GFRP
	2G16-2S12 (D)	180 × 300	30.3	517.0	958.2	226.2	402.1	100.5	45.7	60	35	30	GFRP
Maranan (2019) [58]	2G_2G1S	200 × 300	31.0	500.0	1184.0	200.0	395.8	253.4	62.6	50	50	35	GFRP
	2G_2G2S (D)	200 × 300	31.0	500.0	1184.0	400.0	395.8	253.4	62.6	90	45	35	GFRP
	2G_3G2S (D)	200 × 300	31.0	500.0	1184.0	400.0	593.7	253.4	62.6	90	45	35	GFRP
El Refai(2015) [59]	2G12-1S10	230 × 300	40.0	520.0	1000.0	78.5	226.2	100.5	50.0	55	55	50	GFRP
	2G12-2S10	230 × 300	40.0	520.0	1000.0	157.1	226.2	100.5	50.0	55	55	50	GFRP
	2G12-2S12	230 × 300	40.0	520.0	1000.0	226.2	226.2	100.5	50.0	55	55	50	GFRP
	2G16-2S10	230 × 300	40.0	520.0	1000.0	157.1	402.1	100.5	50.0	55	55	50	GFRP
	2G16-2S12	230 × 300	40.0	520.0	1000.0	226.2	402.1	100.5	50.0	55	55	50	GFRP
	2G16-2S16	230 × 300	40.0	520.0	1000.0	402.1	402.1	100.5	50.0	55	55	50	GFRP
Ge (2015) [60]	FS1	200 × 300	33.6	360.0	880.0	314.0	301.0	100.5	55.0	35	35	35	BFRP
	FS2	200 × 300	33.6	360.0	880.0	393.0	251.0	100.5	55.0	35	35	35	BFRP
	FS3	200 × 300	33.6	360.0	880.0	471.0	201.0	100.5	55.0	35	35	35	BFRP
Kim (2019) [61]	CFRP-40S	150 × 250	40.9	446.0	1655.0	142.6	142.6	142.6	103.0	85	35	35	CFRP
	CFRP-60S	150 × 250	61.7	446.0	1655.0	142.6	142.6	142.6	103.0	85	35	35	CFRP
	GFRP-40S	150 × 250	40.9	446.0	1118.0	142.6	253.4	142.6	48.0	85	35	35	GFRP
	GFRP-60S	150 × 250	61.7	446.0	1118.0	142.6	253.4	142.6	48.0	85	35	35	GFRP

Table A1. *Cont.*

Reference	Beam	$b \times h$ [mm^2]	f'_c [MPa]	f_y [MPa]	f_{fu} [MPa]	A_s [mm^2]	A_f [mm^2]	A'_s [mm^2]	E_f [GPa]	y_s [mm]	y_f [mm]	y'_s [mm]	FRP Type
Wei (2024) [62]	H-A12-C55	180 × 250	56.3	521.2	1306.2	226.2	226.2	100.5	50.1	40	35	35	AFRP
	H-B12-C55	180 × 250	56.3	521.2	912.7	226.2	226.2	100.5	55.6	40	35	35	BFRP
	H-C12-C55	180 × 250	56.3	521.2	2102.1	226.2	226.2	100.5	124.2	40	35	35	CFRP
	H-G10-C55	180 × 250	56.3	521.2	956.4	226.2	157.1	100.5	48.7	40	35	35	GFRP
	H-G12-C55	180 × 250	56.3	521.2	910.6	226.2	226.2	100.5	45.0	40	35	35	GFRP
	H-G14-C55	180 × 250	56.3	521.2	880.6	226.2	307.9	100.5	43.4	40	35	35	GFRP
	H-G16-C55	180 × 250	56.3	521.2	855.7	226.2	402.1	100.5	41.1	40	35	35	GFRP
	H-G12-C30	180 × 250	34.4	521.2	910.6	226.2	226.2	100.5	45.0	40	35	35	GFRP
	H-G12-C40	180 × 250	42.5	521.2	910.6	226.2	226.2	100.5	45.0	40	35	35	GFRP
	H-G12-C50	180 × 250	51.7	521.2	910.6	226.2	226.2	100.5	45.0	40	35	35	GFRP
Thamrin (2022) [15]	BHG-1	125 × 250	20.0	375.0	788.0	265.5	132.7	157.1	43.9	35	35	35	GFRP
	BHG-2	125 × 250	20.0	375.0	788.0	132.7	265.5	157.1	43.9	35	35	35	GFRP
	BHG-3	125 × 250	20.0	375.0	788.0	265.5	132.7	157.1	43.9	35	50	35	GFRP
	BHG-4	125 × 250	20.0	375.0	788.0	132.7	265.5	157.1	43.9	50	35	35	GFRP
	BHC-1	125 × 250	20.0	375.0	2070.0	265.5	132.7	157.1	124.0	35	35	35	CFRP
	BHC-2	125 × 250	20.0	375.0	2070.0	132.7	265.5	157.1	124.0	35	35	35	CFRP
	BHC-3	125 × 250	20.0	375.0	2070.0	265.5	132.7	157.1	124.0	35	50	35	CFRP
	BHC-4	125 × 250	20.0	375.0	2070.0	132.7	265.5	157.1	124.0	50	35	35	CFRP
Kartal (2023) [63]	B1S4	200 × 300	31.3	470.0	1034.0	452.4	59.1	157.1	43.0	40	40	40	BFRP
	B2S3	200 × 300	31.3	470.0	1034.0	339.3	118.3	157.1	43.0	40	40	40	BFRP
	B3S2	200 × 300	31.3	470.0	1034.0	226.2	177.4	157.1	43.0	40	40	40	BFRP
	B4S1	200 × 300	31.3	470.0	1034.0	113.1	236.5	157.1	43.0	40	40	40	BFRP
	G1S4	200 × 300	31.3	470.0	449.0	452.4	129.9	157.1	35.0	40	40	40	GFRP
	G2S3	200 × 300	31.3	470.0	449.0	339.3	259.7	157.1	35.0	40	40	40	GFRP
	G3S2	200 × 300	31.3	470.0	449.0	226.2	389.6	157.1	35.0	40	40	40	GFRP
	G4S1	200 × 300	31.3	470.0	449.0	113.1	519.4	157.1	35.0	40	40	40	GFRP
	G1S5	200.8 × 301.86	30.5	470.0	580.0	565.5	117.4	157.1	46.0	40	40	40	GFRP
	G2S4	199.8 × 301.14	30.5	470.0	580.0	452.4	234.9	157.1	46.0	40	40	40	GFRP
	G3S3	200.6 × 304.43	30.5	470.0	580.0	339.3	352.3	157.1	46.0	40	40	40	GFRP
	G4S2	198.6 × 304.57	30.5	470.0	580.0	226.2	469.7	157.1	46.0	40	40	40	GFRP
	G5S1	200.6 × 306	30.5	470.0	580.0	113.1	587.2	157.1	46.0	40	40	40	GFRP
	B1S2	199.8 × 308	30.5	470.0	1034.0	226.2	59.1	157.1	43.0	40	40	40	BFRP
	B2S1	199.2 × 301.71	30.5	470.0	1034.0	113.1	118.3	157.1	43.0	40	40	40	BFRP
	G1S2	198.6 × 304.86	30.5	470.0	580.0	226.2	117.4	157.1	46.0	40	40	40	GFRP
	G2S1	202 × 301.57	30.5	470.0	580.0	113.1	234.9	157.1	46.0	40	40	40	GFRP

Appendix B. Experimental and Numerical Comparison of Yielding and Ultimate Moments

Table A2 reports the comparison between the experimental and numerical yielding moments and ultimate moments for each specimen in the benchmark database. The numerical-to-experimental ratios are provided for both response quantities. The predicted failure mode is reported in the last column.

Table A2. Comparison between experimental and numerical yielding and ultimate moments.

Reference	Beam	$M_{y,e}$ [kNm]	$M_{y,num}$ [kNm]	$M_{y,num}/M_{y,e}$	$M_{u,e}$ [kNm]	$M_{u,num}$ [kNm]	$M_{u,num}/M_{u,e}$	FM
Aiello (2002) [8]	A1	8.92	8.51	0.95	20.14	21.53	1.07	FM-3
	A2	9.09	9.46	1.04	28.46	27.78	0.98	FM-3
	A3	19.67	17.60	0.89	34.55	35.96	1.04	FM-3
Qu (2009) [9]	C1	8.63	9.28	1.08	22.37	22.74	1.02	FM-3
	B3	20.77	19.21	0.93	40.64	43.84	1.08	FM-3
	B4	18.94	20.67	1.09	39.60	40.00	1.01	FM-3
	B5	20.77	19.21	0.93	40.64	43.84	1.08	FM-3
	B6	30.00	33.48	1.12	42.57	40.15	0.94	FM-3
	B7	73.70	78.67	1.07	73.70	78.67	1.07	FM-3
Lueng (2003) [49]	L2	13.65	10.45	0.77	22.23	17.26	0.78	FM-3
	L5	15.40	11.31	0.73	23.07	19.44	0.84	FM-3
Yoon (2011) [50]	H2	11.90	11.08	0.93	21.11	22.61	1.07	FM-3
	CS	45.60	44.45	0.97	77.60	87.34	1.13	FM-3
	GS	46.00	41.54	0.90	82.00	78.45	0.96	FM-3
Lau (2010) [51]	G0.3-MD1.0-A90	101.85	107.22	1.05	147.00	144.59	0.98	FM-3
	G1.0-T0.7-A90	157.50	154.05	0.98	252.00	238.39	0.95	FM-3
	G0.6-T1.0-A90	183.75	184.10	1.00	229.00	236.30	1.03	FM-3
Mohamed (2013) [52]	B10|8S	13.27	12.88	0.97	14.41	14.97	1.04	FM-3
	B10|6S	12.58	11.44	0.91	14.09	13.25	0.94	FM-3
	B12|8S	14.87	14.75	0.99	16.24	16.89	1.04	FM-3
	B12|6S	13.73	13.61	0.99	14.89	15.79	1.06	FM-3

Table A2. *Cont.*

Reference	Beam	$M_{y,e}$ [kNm]	$M_{y,num}$ [kNm]	$M_{y,num}/M_{y,e}$	$M_{u,e}$ [kNm]	$M_{u,num}$ [kNm]	$M_{u,num}/M_{u,e}$	FM
Hong (2011) [53]	ALII-2	124.50	109.91	0.88	145.50	150.35	1.03	FM-3
	AMI-2	83.34	74.37	0.89	110.25	115.97	1.05	FM-3
	AMIII-2	146.25	145.22	0.99	174.00	187.44	1.08	FM-3
	AMIII-3	150.00	153.65	1.02	180.00	176.54	0.98	FM-3
	BMIV-1	60.00	60.95	1.02	66.75	68.44	1.03	FM-3
	BMIV-2	60.00	62.28	1.04	71.25	75.29	1.06	FM-3
	BMIV-3	63.00	64.77	1.03	78.75	81.01	1.03	FM-3
Almusallam (2013) [54]	RW1F	12.60	11.30	0.90	21.84	19.41	0.89	FM-2
	RW2F	11.25	11.52	1.02	23.03	24.38	1.06	FM-2
Badawi (2009) [55]	NonPrs	35.75	35.25	0.99	53.08	57.65	1.09	FM-3
Wang (2022) [56]	B1.09-S0.25-0.23	18.00	17.81	0.99	45.00	46.31	1.03	FM-3
	B0.75-S0.36-0.48	20.50	19.29	0.94	45.75	42.45	0.93	FM-3
	B0.55-S0.53-0.96	18.90	18.83	1.00	37.50	38.12	1.02	FM-3
	B0.52-S0.52-1.00	17.00	17.61	1.04	40.75	37.66	0.92	FM-3
	B0.35-S0.54-1.56	18.40	19.13	1.04	34.00	33.38	0.98	FM-3
Ruan (2020) [57]	2G12-2S12	40.25	40.90	1.02	57.50	60.03	1.04	FM-3
	2G16-2S12	50.64	51.09	1.01	63.30	59.85	0.95	FM-3
	2G12-1S16	33.84	31.20	0.92	56.40	55.36	0.98	FM-3
	2G16-1S16	40.02	39.93	1.00	66.70	69.48	1.04	FM-3
	2G12-2S12 (D)	37.66	36.76	0.98	53.80	53.10	0.99	FM-3
	2G16-2S12 (D)	38.15	42.25	1.11	50.60	52.67	1.04	FM-3
Maranan (2019) [58]	2G_2G1S	52.30	41.77	0.80	88.55	76.54	0.86	FM-3
	2G_2G2S (D)	69.85	57.40	0.82	88.00	78.85	0.90	FM-3
	2G_3G2S (D)	79.75	65.20	0.82	96.25	87.99	0.91	FM-3
El Refai (2015) [59]	2G12-1S10	15.60	16.62	1.07	47.60	52.15	1.10	FM-3
	2G12-2S10	25.30	26.09	1.03	53.50	57.48	1.07	FM-3
	2G12-2S12	34.06	34.20	1.00	58.90	62.33	1.06	FM-3
	2G16-2S10	30.06	29.60	0.98	73.20	70.62	0.96	FM-3
	2G16-2S12	40.44	38.75	0.96	77.00	74.91	0.97	FM-3
	2G16-2S16	55.60	58.41	1.05	81.40	86.35	1.06	FM-3
Ge (2015) [60]	FS1	37.33	34.81	0.93	74.40	73.90	0.99	FM-3
	FS2	42.45	40.04	0.94	73.50	73.20	1.00	FM-3
	FS3	47.80	45.16	0.94	72.80	72.43	0.99	FM-3
Kim (2019) [61]	CFRP-40S	17.89	19.26	1.08	46.04	44.65	0.97	FM-3
	CFRP-60S	19.98	21.53	1.08	63.61	55.66	0.87	FM-3
	GFRP-40S	19.26	18.27	0.95	41.54	41.48	1.00	FM-3
	GFRP-60S	19.98	19.56	0.98	51.96	51.52	0.99	FM-3
Wei (2024) [62]	H-A12-C55	30.68	30.79	1.00	49.50	51.63	1.04	FM-3
	H-B12-C55	29.31	29.25	1.00	51.00	51.63	1.01	FM-3
	H-C12-C55	32.32	29.80	0.92	65.40	66.36	1.01	FM-3
	H-G10-C55	30.00	30.80	1.03	47.00	45.40	0.97	FM-3
	H-G12-C55	29.60	30.80	1.04	48.06	48.89	1.02	FM-3
	H-G14-C55	31.00	30.80	0.99	52.64	51.63	0.98	FM-3
	H-G16-C55	29.50	28.56	0.97	52.64	53.67	1.02	FM-3
	H-G12-C30	28.09	28.46	1.01	48.56	48.89	1.01	FM-3
	H-G12-C40	28.18	28.49	1.01	45.23	46.79	1.03	FM-3
	H-G12-C50	28.18	28.94	1.03	59.87	58.87	0.98	FM-3
Thamrin (2022) [15]	BHG-1	21.00	20.00	0.95	30.00	27.66	0.92	FM-3
	BHG-2	13.70	13.19	0.96	29.00	27.92	0.96	FM-3
	BHG-3	21.00	20.04	0.95	27.00	25.77	0.95	FM-3
	BHG-4	13.60	14.80	1.09	28.90	30.71	1.06	FM-3
	BHC-1	24.40	21.40	0.88	38.10	37.63	0.99	FM-3
	BHC-2	21.40	20.90	0.98	41.40	37.97	0.92	FM-3
	BHC-3	22.70	21.40	0.94	33.40	31.60	0.95	FM-3
	BHC-4	23.30	21.40	0.92	39.90	36.97	0.93	FM-3
Kartal (2023) [63]	B1S4	56.18	52.40	0.93	70.30	65.00	0.92	FM-3
	B2S3	45.02	42.60	0.95	67.07	64.77	0.97	FM-3
	B3S2	33.24	31.60	0.95	67.04	64.77	0.97	FM-3
	B4S1	23.00	20.43	0.89	71.05	64.77	0.91	FM-3
	G1S4	56.33	53.40	0.95	74.59	66.91	0.90	FM-3
	G2S3	44.13	44.50	1.01	75.27	68.57	0.91	FM-3
	G3S2	33.04	35.06	1.06	74.88	70.32	0.94	FM-3
	G4S1	20.52	23.58	1.15	73.72	72.18	0.98	FM-3
	G1S5	65.79	65.78	1.00	78.19	81.41	1.04	FM-3
	G2S4	61.99	56.50	0.91	81.10	85.15	1.05	FM-3
	G3S3	53.04	48.07	0.91	88.27	89.05	1.01	FM-3
	G4S2	37.17	39.87	1.07	87.40	90.92	1.04	FM-3
	G5S1	30.12	30.12	1.00	85.96	92.47	1.08	FM-3
	B1S2	30.71	29.40	0.96	48.20	45.79	0.95	FM-3
	B2S1	18.63	20.41	1.10	45.51	47.72	1.05	FM-3
	G1S2	30.76	29.40	0.96	49.17	45.26	0.92	FM-3
	G2S1	20.70	19.50	0.94	58.22	48.53	0.83	FM-3

References

1. Schembari, F.; Mairone, M.; Masera, D.; Corrado, M. Comparative Environmental and Economic Performance of Steel- and GFRP-Reinforced Concrete Bridge Decks Under Durability- Based Service Life Scenarios. *Buildings* **2026**, *16*, 1446. [CrossRef]
2. ACI Committee 440. *Building Code Requirements for Structural Concrete Reinforced with Glass Fiber-Reinforced Polymer (GFRP) Bars–Code and Commentary (ACI 440.11-22)*; ACI: Farmington Hills, MI, USA, 2022.
3. Ortiz, J.D.; Dolati, S.S.K.; Malla, P.; Nanni, A.; Mehrabi, A. FRP-Reinforced/Strengthened Concrete: State-of-the-Art Review on Durability and Mechanical Effects. *Materials* **2023**, *16*, 1990. [CrossRef] [PubMed]
4. Hussain, Z.; Lin, J.; Trussoni, M.J.; Nanni, A. Thickness of Glass Fiber-Reinforced Polymer-Reinforced Concrete Slabs. *ACI Struct. J.* **2023**, *120*, 187–196. [CrossRef]
5. Hussain, Z.; Nanni, A. Design and Detailing of Glass Fiber-Reinforced Polymer-Reinforced Concrete Beams According to ACI CODE-440.11-22. *ACI Struct. J.* **2023**, *120*, 179–190. [CrossRef]
6. Mairone, M.; Heydarpour, K.; Alvaro, R.E.; Caso, F.D.; Masera, D.; Corrado, M.; Nolan, S.; Nanni, A. Design of Waterline Pile Cap Footings for Bridges Using Large Diameter GFRP Reinforcing Bars. In *Proceedings of the 12th International Conference on FRP Composites in Civil Engineering (CICE 2025)*; Correia, J.R., Cabral-Fonseca, S., Gonilha, J., Firmo, J., Garrido, M., Eds.; Springer: Cham, Switzerland, 2026; pp. 1704–1714. [CrossRef]
7. Nanni, A.; De Luca, A.; Zadeh, H.J. *Reinforced Concrete with FRP Bars*; CRC Press: London, UK, 2014. [CrossRef]
8. Aiello, M.A.; Ombres, L. Structural Performances of Concrete Beams with Hybrid (Fiber-Reinforced Polymer–Steel) Reinforcements. *J. Compos. Constr.* **2002**, *6*, 133–140. [CrossRef]
9. Qu, W.; Zhang, X.; Huang, H. Flexural Behavior of Concrete Beams Reinforced with Hybrid (GFRP and Steel) Bars. *J. Compos. Constr.* **2009**, *13*, 350–359. [CrossRef]
10. Dziomdziora, P.; Smarzewski, P. Reinforced Concrete Beams with FRP and Hybrid Steel–FRP Composite Bars: Load–Deflection Response, Failure Mechanisms, and Design Implications. *Materials* **2025**, *18*, 4381. [CrossRef]
11. Devaraj, R.; Olofinjana, A.; Gerber, C. Making a Case for Hybrid GFRP-Steel Reinforcement System in Concrete Beams: An Overview. *Appl. Sci.* **2023**, *13*, 1463. [CrossRef]
12. Ibrahim, M.; Asadian, A.; Galal, K. A simplified approach for design of steel-GFRP hybrid reinforced concrete sections. *Eng. Struct.* **2023**, *278*, 115352. [CrossRef]
13. Pang, L.; Qu, W.; Zhu, P.; Xu, J. Design Propositions for Hybrid FRP-Steel Reinforced Concrete Beams. *J. Compos. Constr.* **2016**, *20*, 04015086. [CrossRef]
14. Zhou, B.; Wu, R.Y.; Liu, Y.; Zhang, X.; Yin, S. Flexural Strength Design of Hybrid FRP-Steel Reinforced Concrete Beams. *Materials* **2021**, *14*, 6400. [CrossRef] [PubMed]
15. Thamrin, R.; Zaidir, Z.; Iwanda, D. Ductility Estimation for Flexural Concrete Beams Longitudinally Reinforced with Hybrid FRP–Steel Bars. *Polymers* **2022**, *14*, 1017. [CrossRef]
16. Araba, A.M.; Zinkaah, O.H.; Alhawat, M.; Ashour, A. Experimental tests of two span continuous concrete beams reinforced with hybrid GFRP-Steel bars. *Structures* **2023**, *47*, 2485–2500. [CrossRef]
17. Almahmood, H.; Ashour, A.; Sheehan, T. Flexural behavior of hybrid steel-GFRP reinforced concrete continuous T-beams. *Compos. Struct.* **2020**, *254*, 112802. [CrossRef]
18. Elkafrawy, M.; Gowrishankar, P.; Aswad, N.G.; Alashkar, A.; Khalil, A.; AlHamaydeh, M.; Hawileh, R. GFRP-Reinforced Concrete Columns: State-of-the-Art, Behavior, and Research Needs. *Buildings* **2024**, *14*, 3131. [CrossRef]
19. Tarantini, R.; Mairone, M.; Ferro, G.A.; Corrado, M.; Givonetti, M.; Gallina, G.; Masera, D. Seismic Vulnerability Assessment of RC Bridge Piers Strengthened with GFRP Rebars: A Case Study. In *Engineering Materials, Structures, Systems and Methods for a More Sustainable Future*; Zingoni, A., Ed.; CRC Press: London, UK, 2025. [CrossRef]
20. Kara, I.F.; Ashour, A.F.; Köroğlu, M.A. Flexural behavior of hybrid FRP/steel reinforced concrete beams. *Compos. Struct.* **2015**, *129*, 111–121. [CrossRef]
21. Duy, N.P.; Tan, N.N.; Hiep, D.V. Failure mode classification for hybrid FRP/steel reinforced concrete beams: A soft computing concept based on the numerical model. *Innov. Infrastruct. Solut.* **2024**, *9*, 288. [CrossRef]
22. Osman, S.M.S.; Aldabagh, S.; Alam, M.S.; Sheikh, S.A. Performance-Based Seismic Design of Hybrid GFRP–Steel Reinforced Concrete Bridge Columns. *J. Compos. Constr.* **2023**, *27*, 04023011. [CrossRef]
23. Ibrahim, H.A.; Fahmy, M.F.; Wu, Z. Numerical study of steel-to-FRP reinforcement ratio as a design-tool controlling the lateral response of SFRC beam-column joints. *Eng. Struct.* **2018**, *172*, 253–274. [CrossRef]
24. Fossetti, M.; Papia, M. Dimensionless analysis of RC rectangular sections under axial load and biaxial bending. *Eng. Struct.* **2012**, *44*, 34–45. [CrossRef]
25. Carpinteri, A.; Corrado, M.; Goso, G.; Paggi, M. Size-scale effects on interaction diagrams for reinforced concrete columns. *Constr. Build. Mater.* **2012**, *27*, 271–279. [CrossRef]
26. Araba, A.M.; Ashour, A.F. Flexural performance of hybrid GFRP-Steel reinforced concrete continuous beams. *Compos. Part B Eng.* **2018**, *154*, 321–336. [CrossRef]

27. Magliulo, G.; Tuozzo, F.; D'Angela, D.; Salvatore, C.D.; Nanni, A. GFRP reinforcement in RC structures in seismic zones. *Structures* **2025**, *82*, 110589. [CrossRef]
28. Magliulo, G.; Tuozzo, F.; D'Angela, D.; Di Salvatore, C.; Nanni, A. Structural design and assessment of hybrid GFRP-steel RC beams in seismic areas. *Bull. Earthq. Eng.* **2026**. [CrossRef]
29. Zou, P.X.W. Flexural Behavior and Deformability of Fiber Reinforced Polymer Prestressed Concrete Beams. *J. Compos. Constr.* **2003**, *7*, 275–284. [CrossRef]
30. Mairone, M.; Givonetti, M.; Hussain, Z.; Gallina, G.; Corrado, M.; Nanni, A.; Masera, D. Ultimate Limit State Behavior of RC Members in Bending Strengthened with GFRP Rebars. In *Proceedings of the Resilience, Earthquake Engineering and Structural Health Monitoring*; Cimellaro, G.P., Zhou, Y., Cardoni, A., Ansari, F., Eds.; Springer: Cham, Switzerland, 2025; pp. 313–329. [CrossRef]
31. *EN 1992-1-1*; Eurocode 2: Design of Concrete Structures—Part 1-1: General Rules and Rules for Buildings, Bridges and Civil Engineering Structures. European Committee for Standardization: Brussels, Belgium, 2005.
32. *ACI 318M-25*; Building Code for Structural Concrete—Code Requirements and Commentary. American Concrete Institute: Farmington Hills, MI, USA, 2025.
33. *CNR-DT 203 R1/2026*; Guidelines for the Design, Execution and Inspection of Reinforced Concrete Structures with Fiber-Reinforced Polymer (FRP) Bars. National Research Council of Italy: Rome, Italy, 2026.
34. AASHTO LRFD. *Bridge Design Guide Specifications for GFRP-Reinforced Concrete*, 2nd ed.; American Association of State Highway and Transportation Officials: Washington, DC, USA, 2018.
35. *CSA S806-12*; Design and Construction of Building Structures with fiber-Reinforced Polymers. Canadian Standards Association: Mississauga, ON, Canada, 2012.
36. *ASTM D7957/D7957M-22*; Standard Specification for Solid Round Glass Fiber Reinforced Polymer Bars for Concrete Reinforcement. ASTM International: West Conshohocken, PA, USA, 2022.
37. *ASTM D8505/D8505M-23*; Standard Specification for Basalt and Glass Fiber Reinforced Polymer (FRP) Bars for Concrete Reinforcement. ASTM International: West Conshohocken, PA, USA, 2023.
38. Nouri, Y.; Ghanbari, M.A.; Fakharian, P. Flexural behavior of hybrid GFRP-steel reinforced concrete beam: Experimental and explainable artificial intelligence. *Eng. Struct.* **2025**, *345*, 121565. [CrossRef]
39. Hussain, Z.; Tuozzo, F.; Magliulo, G.; Nanni, A. Hybrid Reinforced Concrete Cross-Section Using Fiber-Reinforced Polymer and Steel Bars. *Int. J. Concr. Struct. Mater.* **2025**, *19*, 26. [CrossRef]
40. Peng, F.; Deng, J.; Xue, W. Design Provisions for Flexural Strength of Hybrid Reinforced Concrete Beams with Fiber-Reinforced Polymer and Steel Bars. *ACI Struct. J.* **2023**, *120*, 49–59. [CrossRef]
41. Tarawneh, A.; Alajarmeh, O.; Alawadi, R.; Amirah, H.; Alramadeen, R. Database evaluation and reliability calibration for flexural strength of hybrid FRP/steel–RC Beams. *Compos. Struct.* **2024**, *329*, 117758. [CrossRef]
42. AlAjarmeh, O.S.; Manalo, A.C.; Benmokrane, B.; Vijay, P.V.; Ferdous, W.; Mendis, P. Novel testing and characterization of GFRP bars in compression. *Constr. Build. Mater.* **2019**, *225*, 1112–1126. [CrossRef]
43. Elmessalami, N.; Refai, A.E.; Abed, F. Fiber-reinforced polymers bars for compression reinforcement: A promising alternative to steel bars. *Constr. Build. Mater.* **2019**, *209*, 725–737. [CrossRef]
44. Ye, Y.Y.; Zhuge, Y.; Smith, S.T.; Zeng, J.J.; Bai, Y.L. Behavior of GFRP-RC columns under axial compression: Assessment of existing models and a new axial load-strain model. *J. Build. Eng.* **2022**, *47*, 103782. [CrossRef]
45. Mirdarsoltany, M.; Roghani, H.; Masoule, M.S.T.; Khodadadi, N.; Ghahremaninezhad, A.; Nanni, A. Evaluating GFRP bars under axial compression and quantifying load-damage correlation. *Constr. Build. Mater.* **2023**, *409*, 133945. [CrossRef]
46. Bulmer, M.G. *Principles of Statistics*, revised ed.; Dover Publications: New York, NY, USA, 1979.
47. Khodadadi, N.; Golafshani, E.; Roghani, H.; Behnood, A.; El-kenawy, E.S.M.; Ngo, T.; Nanni, A. Predicting the Compressive Strength of Glass Fiber-Reinforced Polymer Confined-Concrete Elements Using Metaheuristics-Guided Machine Learning. *Int. J. Concr. Struct. Mater.* **2025**, *19*, 105. [CrossRef]
48. Khodadadi, N.; Roghani, H.; De Caso, F.; El-kenawy, E.S.M.; Yesha, Y.; Nanni, A. Machine learning approach for the flexural strength of 3D-printed fiber-reinforced concrete based on the meta-heuristic algorithm. *Struct. Concr.* **2025**, *26*, 4103–4142. [CrossRef]
49. Leung, H.Y.; Balendran, R.V. Flexural behavior of concrete beams internally reinforced with GFRP rods and steel rebars. *Struct. Surv.* **2003**, *21*, 146–157. [CrossRef]
50. Yoon, Y.S.; Yang, J.M.; Min, K.H.; Shin, H.O. Flexural strength and deflection characteristics of high-strength concrete beams with hybrid FRP and steel bar reinforcement. In *Proceedings of the 10th International Symposium on Fiber-Reinforced Polymer Reinforcement for Concrete Structures, FRPRCS-10*; ACI Special Publication SP-275; ACI: Farmingto Hills, MI, USA, 2011; pp. 1–22.
51. Lau, D.; Pam, H.J. Experimental study of hybrid FRP reinforced concrete beams. *Eng. Struct.* **2010**, *32*, 3857–3865. [CrossRef]
52. Safan, M.A. Flexural Behavior and Design of Steel-GFRP Reinforced Concrete Beams. *ACI Mater. J.* **2013**, *110*, 677–685. [CrossRef]
53. Hong, K.N.; Han, J.W.; Seo, D.W.; Han, S.H. Flexural response of reinforced concrete members strengthened with near-surface-mounted CFRP strips. *Int. J. Phys. Sci.* **2011**, *6*, 948–961.

54. Almusallam, T.H.; Elsanadedy, H.M.; Al-Salloum, Y.A.; Alsayed, S.H. Experimental and numerical investigation for the flexural strengthening of RC beams using near-surface mounted steel or GFRP bars. *Constr. Build. Mater.* **2013**, *40*, 145–161. [CrossRef]
55. Badawi, M.; Soudki, K. Flexural strengthening of RC beams with prestressed NSM CFRP rods - experimental and analytical investigation. *Constr. Build. Mater.* **2009**, *23*, 3292–3300. [CrossRef]
56. Wang, X.; Liu, S.; Shi, Y.; Wu, Z.; He, W. Integrated High-Performance Concrete Beams Reinforced with Hybrid BFRP and Steel Bars. *J. Struct. Eng.* **2022**, *148*, 04021235. [CrossRef]
57. Ruan, X.; Lu, C.; Xu, K.; Xuan, G.; Ni, M. Flexural behavior and serviceability of concrete beams hybrid-reinforced with GFRP bars and steel bars. *Compos. Struct.* **2020**, *235*, 111772. [CrossRef]
58. Maranan, G.B.; Manalo, A.C.; Benmokrane, B.; Karunasena, W.; Mendis, P.; Nguyen, T.Q. Flexural behavior of geopolymer-concrete beams longitudinally reinforced with GFRP and steel hybrid reinforcements. *Eng. Struct.* **2019**, *182*, 141–152. [CrossRef]
59. Refai, A.E.; Abed, F.; Al-Rahmani, A. Structural performance and serviceability of concrete beams reinforced with hybrid (GFRP and steel) bars. *Constr. Build. Mater.* **2015**, *96*, 518–529. [CrossRef]
60. Ge, W.; Zhang, J.; Cao, D.; Tu, Y. Flexural behaviors of hybrid concrete beams reinforced with BFRP bars and steel bars. *Constr. Build. Mater.* **2015**, *87*, 28–37. [CrossRef]
61. Kim, S.; Kim, S. Flexural behavior of concrete beams with steel bar and FRP reinforcement. *J. Asian Archit. Build. Eng.* **2019**, *18*, 89–97. [CrossRef]
62. Wei, B.; He, X.; Zhou, M.; Wang, H.; He, J. Experimental study on flexural behaviors of FRP and steel bars hybrid reinforced concrete beams. *Case Stud. Constr. Mater.* **2024**, *20*, e02759. [CrossRef]
63. Kartal, S.; Kalkan, I.; Mertol, H.C.; Baran, E. Influence of the proportion of FRP to steel reinforcement on the strength and ductility of hybrid reinforced concrete beams. *Eur. J. Environ. Civ. Eng.* **2023**, *27*, 3546–3565. [CrossRef]

Disclaimer/Publisher's Note: The statements, opinions and data contained in all publications are solely those of the individual author(s) and contributor(s) and not of MDPI and/or the editor(s). MDPI and/or the editor(s) disclaim responsibility for any injury to people or property resulting from any ideas, methods, instructions or products referred to in the content.